

TITLE

GAS GEOCHEMISTRY AT GRANDE COMORE AND MAYOTTE VOLCANIC ISLANDS (COMOROS ARCHIPELAGO), INDIAN OCEAN

Marco Liuzzo^(1,7), Andrea Di Muro^(2,3), Andrea Luca Rizzo⁽¹⁾, Antonio Caracausi⁽¹⁾, Fausto Grassa⁽¹⁾, Nicolas Fournier⁽⁴⁾, Bafakih Shafik⁽⁵⁾, Guillaume Boudoire^(1,6), Massimo Coltorti⁽⁷⁾, Manuel Moreira⁽⁸⁾, Francesco Italiano⁽¹⁾

⁽¹⁾ Istituto Nazionale di Geofisica e Vulcanologia, Sezione di Palermo – Italy,

⁽²⁾ Université de Paris, Institut de physique du globe de Paris, CNRS, F-75005 Paris, France

⁽³⁾ Observatoire volcanologique du Piton de la Fournaise, Institut de physique du globe de Paris, F-97418 La Plaine des Cafres, France

⁽⁴⁾ GNS Science, New Zealand,

⁽⁵⁾ Observatoire Volcanologique du Karthala - CNDRS, Comoroès,

⁽⁶⁾ Université Clermont Auvergne, CNRS, IRD, OPGC, Laboratoire Magmas et Volcans, F-63000 Clermont-Ferrand, France,

⁽⁷⁾ Università di Ferrara, Dipartimento di Fisica e Scienze della Terra – Italy,

⁽⁸⁾ ISTO, Institut de Sciences de la Terre d'Orléans, France

Corresponding author: Marco Liuzzo (marco.liuzzo@ingv.it)

Key Points:

- Map of the spatial distribution of ground CO₂ emissions and its isotopic characteristics in both islands Grande Comore and Mayotte
- Geochemical characterisation of fumarolic and hydrothermal gases in terms of both primary component species and isotopic characteristics
- Correlation between the variability of geochemical tracers and the new submarine volcano off Mayotte and its implications for the risk to the island's inhabitants

Abstract

The Comoros Archipelago is an active geodynamic region of intra-plate volcanism within which the youngest and oldest islands (Grande Comore and Mayotte respectively) are characterized by recent volcanic activity. The frequent eruptions of the large shield volcano Karthala on Grande Comore (last eruption 2007), and the recent birth of a large submarine volcano since 2018 at the submarine base of Mayotte are associated with permanent fumarolic emissions, bubbling gas seeps, and soil gas emissions, which are studied in detail here for the first time. CO₂ fluxes and chemical and isotopic gas compositions acquired during two surveys in 2017 and 2020 are

integrated with older datasets collected between 2005 and 2016, permitting the identification of a possible influence of the recent volcanic and magmatic activity at Mayotte.

At Karthala, high gas fluxes with high temperature, and a marked magmatic signature are concentrated close to the summit crater area, while only weaker emissions with a stronger biogenic signature are found on the volcano flanks. At Mayotte, lower temperature and higher CH₄ content are recorded in two main seep areas of CO₂-rich fluid bubbling, while soil emissions on land record a higher proportion of magmatic fluids compared to Karthala. Our preliminary results reveal two quite separate gas emission patterns for each island that are distinct in composition and isotopic signatures, and well-correlated with the present state of volcanic activity. This work may potentially provide support for local observation infrastructures and contribute to the improvement in volcanic and environmental monitoring.

1. Introduction

Comoros archipelago is located in the Mozambique Channel between the east coast of Africa and the north-western coast of Madagascar. The formation of a huge submarine volcanic edifice since 2018, about 50 km offshore east of Mayotte, has prompted a renewal of multidisciplinary researches on the seismo-volcanic activity of the Comoros Archipelago by the international volcanological community (Bachèlery et al., 2019; Berthod et al., 2020; Cesca et al., 2020; Feuillet et al., 2019; Lemoine et al., 2020; REVOSIMA, 2019). The archipelago consists of four main islands from NW to SE: Grande Comore, Mohéli, Anjouan, and Mayotte (Figure 1), amongst which Grande Comore hosts the large and frequently active basaltic Karthala volcano (last eruption in 2007). Subaerial Holocene volcanic activity related to a range of alkaline magma compositions (from basanite to phonolite) has been documented in the other islands (Bachèlery et al., 2016; Michon et al., 2016; Tzevahirtzian et al., 2021 and references therein). Comoros Archipelago is considered as the potential diffuse Lwandle-Somali sub-plate boundary and part of the SE extension of the East African Rift System (Michon et al., 2016; Famin et al., 2020). The recent review of morphological, geological and chronological data of Tzevahirtzian et al. (2021) suggests that Mayotte and Moheli are the oldest islands, while Anjouan and Grande Comore are the most recent ones. The recent volcanism of Karthala in Grande Comore has been interpreted as hot-spot-related by geochemical studies (e.g. Class et al., 1998). Grande Comore and Anjouan are high altitude volcanic islands, intersected by well developed triple-armed volcanic rifts. On the contrary, Moheli and Mayotte are lower islands, with less well developed rift zones, and a wide insular shelf, which is very narrow on Grande Comore and Anjouan. Karthala is the second most

67 active volcano in the Indian Ocean, after Piton de la Fournaise in La Réunion island, with
68 permanent hydrothermal and fumarolic emissions close to its summit area (Bachelery et al., 1996;
69 Bernabeu et al., 2018). Two years after the last summit Karthala eruption, Bernabeu et al. (2018)
70 document high CO₂ fluxes in the soil close to the eruptive vent. However, the absence of chemical
71 or isotopic analysis did not permit to attribute these emissions to the recently emplaced magma or
72 to deeper sources. Seep areas of low-temperature CO₂-rich bubbling gases have been reported for
73 the first time between 1993 and 1998 at Mayotte, on the small island (Petite Terre) located on its
74 eastern side (Traineau et al., 2006 and references therein).

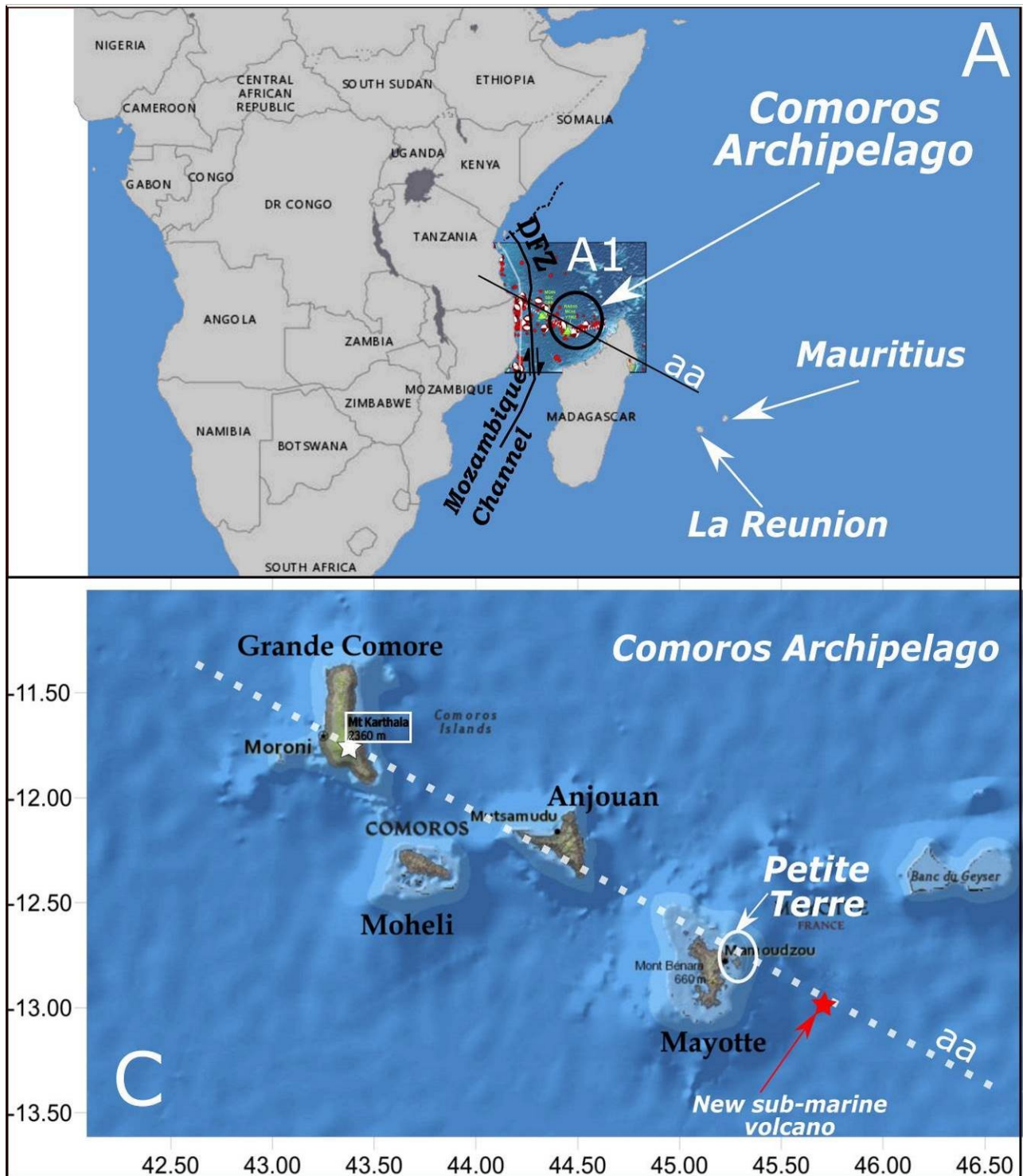


Figure 1. Map of the Comoros Archipelago, which is located on the northern zone of the Mozambique Channel (A), in which is also shown the Davie Fracture zone (DFZ). The elongated trend N120° “a-a” of the islands corresponding with the recognised regional structural trend well defined by distribution of the 1901–2018 seismicity for $M > 4$ showed in the inset A1 (from Lemoine et al., 2020 modified). In (B) highlighted on the map is the little island on the east coast of Mayotte called Petite Terre, where have been acquired all the measurements (both from the soil and from the bubbling area on the sea) mentioned in this paper regarding Mayotte island. The white star at Grande Comore indicates the Karthala volcano. The red star is the approximate location of the new submarine volcano.

In this work, we focus on the gaseous emissions on the oldest (Mayotte) and youngest (Grande Comore) islands, which are also the two recently active volcanic systems of the Comoros

85 archipelago, with the aim at constraining the extent and spatial distribution of the outgassing
86 areas and the geochemical signature of the gas emissions. Data were collected by a team of
87 researchers from IPGP/OVPF and INGV who carried out surveys on the two islands between 2017
88 and 2019. In addition, we included data from older measurement campaigns which were
89 undertaken for different purposes between 2005 and 2014. The results of the geochemical
90 investigation highlight the differences in outgassing characteristics between the two volcanic
91 islands and their link with the recent volcanic activity. We perform a comparison with the gas
92 geochemistry of La Réunion island, where a deep and plume-like undegassed mantle contribution
93 has been since long identified.

94 Grande Comore and Mayotte are densely populated islands and in view of the high level of seismic
95 and volcanic activity and the related hazards, these first results represent a significant contribution
96 to pave the way for future activities on geochemical monitoring and hazard mitigation.

97

98 2. Geological context

99 The islands of the Comorian archipelago are located within the Mozambique Channel in a
100 particularly complex geodynamic region where the tectonic features are yet to be unambiguously
101 defined. The main and better known tectonic structure, the Davie Fracture Zone (DFZ) (Phethean
102 et al., 2016), is considered the kinematic hinge that allowed the southward drift of Madagascar
103 following the Gondwana breakup. Despite its well defined structure, the DFZ has been described
104 as either a western transform fault (Coffin et al., 1986) or as a continent-ocean transform margin
105 (Gaina et al., 2013) of the Western Somali Basin (Figure 1A). The alignment of the islands is NW-SE
106 and coincident with the main seismic zone of the archipelago (Figure 1 B - from Lemoine et al.,
107 2020, modified). This orientation of islands separates the North Somali basin, which is agreed to
108 be oceanic, and the South Somali basin, which for some authors is thought to be oceanic crust
109 (e.g. Klimke et al., 2016; Rabinowitz et al., 1983), while other authors identify this as a thinned
110 continental crust (e.g. Bassias & Leclaire, 1990; Roach et al., 2017).

111 The two main hypotheses that have been developed over time to explain the origin of the
112 Comoros volcanism are:

- 113 a) a mantle plume, which interacts with the oceanic lithosphere (Claude-Ivanaj et al., 1998;
114 Class et al., 2005; Deniel, 1998; Nougier et al., 1986; Emerick and Duncan, 1982; Hajash and

Armstrong, 1972). The link with a deep mantle hot spot has been invoked to explain the eastward migration of volcanism age, but also to explain the variability of geochemical magma composition measured along the Archipelago. Karthala lavas are those recording a stronger hot spot signature (Bachèlery and Hémond, 2016; Claude-Ivanaj et al., 1998; Class et al., 2009; Coltorti et al., 1999). Recent seismic tomography (French and Romanowicz, 2015) fails to unambiguously identify a deep plume rooted in the mantle below Comoros archipelago.

- b) the reactivation of regional lithospheric structures, which interact with asthenospheric processes. This hypothesis rejects the previous model because it is inconsistent with the current volcanic activity which includes both Karthala volcano and the recent and still ongoing submarine volcanic activity eastward of Mayotte and with the absence of a clear age decrease along the archipelago (Tzevahirtzian et al., 2021; Famin et al., 2020; Lemoine et al., 2020; Michon, 2016; Nougier et al., 1986)

At Mayotte, the volcanic activity becomes increasingly older from the eastern side (Petite Terre island), to the western main island (Grande Terre) (Nehlig et al., 2013). The still ongoing (at the time of writing), large-volume and long-lasting sub-marine eruption of Mayotte, the largest submarine event ever detected by monitoring networks (Cesca et al., 2020; Lemoine et al., 2020), challenges current models on the origin of Comoros volcanism. Since 2018, several km³ of evolved basanite lava have been emitted on the 3.5 km deep seafloor 50 km east from Mayotte from a deep source located in the upper lithospheric mantle (Bachèlery et al., 2019; Berthod et al., 2020; Lemoine et al. 2020). The new volcano grows on a N120° oriented volcanic ridge, which runs along the eastern submarine flank of Mayotte and whose western subaerial tip is the small island of Petite Terre (Tzevahirtzian et al., 2021; Figure 1C). On Petite Terre, recent volcanic activity has built on the coral reef a set of Holocene basaltic scoria cones and phonolitic maars (Zinke et al., 2001; Nehlig et al., 2013), and two main areas of low-temperature CO₂-rich gas bubbling seeps. A first bubbling area occurs in the NE part of Petite Terre inside the intracrateric lake of the Dziani phonolitic maar, where several CO₂- and CH₄- rich bubbling spots have been identified (Milesi et al., 2020). A second area, first described in 1998 on the eastern tidal flat of Petite Terre is located close to the “Airport beach” (BAS site; Traineau, 2006; Sanjuan, 2008). There, tens of bubbling spots occur at the southern feet of the large “Vigie” phonolitic maar, on a muddy flat area exposed to significant tide and extended for about 250x300m from the beach (see also Figure 8A-8C).

146 In Grande Comore, at least three volcanic massifs have been identified: the old and inactive
147 M'Badjini massif in the southernmost part of Grande Comore, the rarely active La Grille volcano in
148 the north (last dated eruption: 1029-1424 CE) and in between the frequently active Karthala shield
149 volcano (last eruption: 2007) (Bachelery et al., 2016 and references therein). Karthala volcano is a
150 large (summit elevation 2361 m) basaltic shield volcano, the highest relief of the Comoros
151 Archipelago, and exhibits well-developed rift zones diverging from a 3.6 x 2.7 km wide summit
152 polylobate caldera. The average frequency of its eruptions, occurring both at the volcano summit
153 and on the flanks, is of one eruption every 6-8 years over the past 100 years and the volcano was
154 frequently active in the 1991-2007 period (Bachelery et al., 2016). The self-potential study of the
155 summit caldera performed by Lénat et al. (1998) and Bernabeu et al. (2018) show that the main
156 hydrothermal activity of the volcano does not occur below the main summit crater (Choungou-
157 Chahalé), but on the northern part of the summit caldera, where several recent eruptions have
158 occurred. We sampled two main areas, the first one correspond to steaming grounds and
159 fumaroles located close to the Choungou-Chagnoumeni pit crater located in the northern part of
160 the caldera and filled by the lavas of the last eruption in 2007 (see Figure 7B site CC) and a second
161 one, the "Soufrière" fumarolic area located on recent lavas 1.7 km north of the summit caldera,
162 along the northern rift zone (see Figure 7B site LS).

163

164 3. Materials and Methods

165 3.1 Previous datasets

166 In this study, we present the results of our 2017-2020 surveys on soil gas fluxes and their
167 composition as well as on the composition of Mayotte gas bubbling and Grande Comore fumarolic
168 areas (Figures 7 and 8). Our dataset is integrated with older and partly unpublished surveys
169 acquired on the two islands.

170 At Mayotte, the BAS bubbling site has been first studied by BRGM in November 2005 (Traineau,
171 2006; BRGM report) and April 2008 (Sanjouan, 2008; BRGM report) in terms of spatial distribution,
172 gas fluxes, temperature, pH and chemical and isotopic composition. In the BRGM campaigns, $\delta^{13}\text{C}$
173 and dD data were not acquired on methane and preliminary noble gases data were produced by
174 the IPGP laboratory (M. Moreira). A rich biological, chemical and isotopic dataset (C-H-S species,
175 not including the noble gases) of the Dziani intracrateric lake and of its bubbling was acquired in
176 the period 2012-2018 (Jovovic et al., 2017; Leboulanger et al., 2017; Gérard et al., 2018; Hugoni et

177 al., 2018; Milesi et al., 2019; 2020; Cadeau et al., 2020). Milesi et al. (2020) collected fluids in
178 August 2016 by focusing on the spatial distribution and C-H chemical and isotopic composition of
179 bubbling gases in the Dziani lake, while only a single analysis (G7 sample) is reported for the BAS
180 area.

181 On Karthala volcano, the summit steaming grounds and fumarole have been first described (but
182 not sampled) by Bachelery and Coudray (1993). Soil CO₂ and temperature profiles were measured
183 between March 2008 and January 2010 in the hot grounds (40-80°C) close to the summit 2007 pit
184 crater by Bernabeu et al. (2018). The first detailed study of the gas emissions in Grande Comore
185 was performed in 2014 in the frame of an international geothermal exploration project
186 (Benavente et al., 2015; Chaheire et al., 2016).

187

188 **3.2 Gas sampling and analysis**

189 Grande Comore field works were performed in December 2017 (volcano flanks) and October 2018
190 (volcano flanks and summit area). Mayotte surveys were carried out on Petite Terre (Figure 1) in
191 four campaigns, i.e. in December 2018, April 2019, September 2019 and November 2020 (Table 1).

192 Soil gas samples for isotopic ($\delta^{13}\text{C}$ in CO₂) and chemistry analysis were collected by introducing a
193 steel probe into the ground (50 cm long) and collected in 10 mL Exetainer glass vials and in two-
194 stopcock glass bottles 100mL.

195 Dry gases from fumarolic fields at Karthala were collected using a steel probe (the same as for soil
196 sampling) introduced into the ground and connected to a three-way valve equipped of a syringe
197 and a tube connected to the bottles for gas storage. Bubbling gases at Mayotte have been taken
198 using a steel funnel connected to a three-way valve equipped of a syringe and a tube connected to
199 two-stopcock glass bottles 250mL (chemistry and C-H isotopic analysis), two-stopcock steel bottles
200 100mL (noble gases elemental and isotopic analysis), and pre-weighed evacuated bottles
201 containing absorbing alkaline solution (4N NaOH) following the method of Giggenbach and Goguel
202 (1989).

203 All the gas samples were analysed at the laboratories of INGV (Istituto Nazionale di Geofisica e
204 Vulcanologia), Sezione di Palermo, for their chemistry and for the isotopic compositions of noble
205 gases (He, Ne, and Ar), C of CO₂, and C and H of CH₄. Analyses are reported in Table 3. The chemical
206 composition of He, H₂, O₂, N₂, CO, CH₄, and CO₂ was measured by a gas chromatograph (Clarus 500,

207 Perkin Elmer) equipped with a 3.5-m column (Carboxen 1000) and double detector (hot-wire
208 detector and flame ionization detector [FID]), for which the analytical errors were < 3%.

209 The C-isotope composition of CO₂ (expressed as δ¹³C ‰) vs. V-PDB (Vienna-Pee Dee Belemnite)
210 was determined using a continuous-flow isotope-ratio mass spectrometer (Thermo Delta Plus XP,
211 Finnigan), connected to a gas chromatograph (Trace GC) and interface (Thermo GC/C III, Finnigan).
212 The gas chromatograph and its column (length = 30 m and i.d. = 0.32 mm; Poraplot-Q) were
213 operated at a constant temperature of 50°C using He as the carrier gas. The analytical errors were
214 <0.1‰. The same instrument has been used for C and H isotope determination in CH₄, where a
215 combustion interface (Thermo GC III, Finnigan) was used to produce CO₂ from CH₄ and a gas-
216 chromatograph/thermal-conversion interface provided online high-temperature conversion of CH₄
217 into H. The SDs for the δ¹³C and δD measurements of CH₄ were <0.2 and <2.5‰, respectively.

218 Noble gas (He, Ne, Ar) isotopes were analyzed at the noble-gas laboratory at INGV-Palermo. ³He
219 and ⁴He were measured into a split flight tube mass spectrometer (GVI-Helix SFT), after
220 purification of the sample from the major gaseous species and separation from the other noble
221 gases. ²⁰Ne was determined by admitting Ne into a multicollector mass spectrometer (Thermo-
222 Helix MC plus), after purification procedure into a stainless steel ultra-high vacuum line distinct
223 from that of He and Ar, as above described for helium. The ³He/⁴He ratio is expressed as R/R_a
224 (being R_a the He isotope ratio of air and equal to 1.39·10⁻⁶) with an analytical uncertainty (1σ)
225 below 0.3%. Hereafter we discuss the ³He/⁴He ratio corrected for atmospheric contamination
226 using the measured ⁴He/²⁰Ne ratio (e.g., Sano and Wakita, 1985) that is reported in units of R_c/R_a,
227 as follows:

$$228 \quad \frac{R}{R_a} = \frac{\left(\frac{R_m}{R_a}\right) \cdot \left(\frac{{}^4\text{He}}{{}^{20}\text{Ne}}\right)_m - \left(\frac{{}^4\text{He}}{{}^{20}\text{Ne}}\right)_a}{\left(\frac{{}^4\text{He}}{{}^{20}\text{Ne}}\right)_m - \left(\frac{{}^4\text{He}}{{}^{20}\text{Ne}}\right)_a} \quad (1)$$

229 where subscripts *m* and *a* refer to measured and atmosphere theoretical values, respectively [(He/
230 Ne)_a = 0.318] (Ozima and Podosek, 1983). We highlight that the correction on the ³He/⁴He ratio is
231 small or negligible for most of the gas samples [(⁴He/²⁰Ne)_m >> (⁴He/²⁰Ne)_a].

232 The Ar elemental and isotopic composition (³⁶Ar, ³⁸Ar, and ⁴⁰Ar) were quantified in a multicollector
233 mass spectrometer (Helix MC-GVI). The analytical uncertainty (1σ) for single ⁴⁰Ar/³⁶Ar

measurements was <0.1%. ^{40}Ar was corrected for air contamination ($^{40}\text{Ar}^*$) in samples showing $^{40}\text{Ar}/^{36}\text{Ar} > 315$ assuming that the ^{36}Ar present derived from atmosphere, as follows:

$$^{40}\text{Ar}^i = ^{40}\text{Ar}_{\text{sample}} - \text{Ar}_{\text{sample}} \cdot \frac{^{40}\text{Ar}^i}{^{36}\text{Ar}^i} \quad (2)$$

Typical blanks for He, Ne, and Ar were $<10^{-15}$, $<10^{-16}$, and $<10^{-14}$ mol, respectively, and are at least two orders of magnitude lower than the sample signals at the relative mass spectrometers. Further details on samples purification and analysis are described by Rizzo et al. (2019) and Boudoire et al (2020).

3.3 Soil CO₂ fluxes

The soil CO₂ emissions data presented in this study have been acquired drawing on two different methods: accumulation chamber (Chiodini et al. 1998) and dynamic concentration (Gurrieri and Valenza, 1988). The methods differ owing to the fact that different teams carried out measurement surveys on different islands at different times. However, each single measurement campaign is consistent for the method used (Table 1).

3.3.1 Accumulation chamber method

Both Benavente et al. (2015) surveys in Grande Comore and two of our surveys at Mayotte (September 2019 and November 2020) adopted the accumulation chamber method for measurements of soil CO₂ flux emissions using a West Systems portable accumulation chamber equipped with two different IR spectrometers. Benavente's campaign used a West System portable instrument with a LI-COR 820 IR and a 200 mm diameter chamber (West System chamber B), which introduces soil gas through the infrared spectrometer via tubing with an inline Mg(ClO₄)₂ filter (avoiding the absorption of moisture which may cause interference in CO₂ concentration). Our campaigns in 2019 and 2020 at Mayotte Island used a West Systems portable accumulation chamber equipped with a Dräger Polytron IR sensor and a chamber with the same geometry as the one used by Benavente in Grande Comore (West system chamber B). We recorded soil temperature at each measurement location using a handheld Type K thermocouple probe inserted to 10 cm below ground level. In addition, pressure measurements and other weather parameters were recorded by a hand-held instrument meter (Kestrel 5000 series). Soil CO₂ flux ($\text{g m}^{-2} \text{d}^{-1}$) from each site were calculated using the following equation (1):

$$\text{CO}_2 = 44.01 \cdot \frac{86400 \cdot P}{10^6 \cdot R \cdot T_k} \cdot \frac{V}{A} \cdot \frac{\delta_c}{\delta_t} \quad (3)$$

264 where δ_c/δ_t is the change in the CO₂ concentration with time (ppm s⁻¹), P is the measured pressure
265 in mbar, R is the gas constant (bar L K⁻¹ mol⁻¹), T is the measured temperature (K), V is the chamber
266 net volume (0.006186 m³) and A is chamber inlet net area (0.0314 m²). The measurement accuracy
267 of the CO₂ flux measurements method is ± 12.5 % (Evans et al., 2001)

268 3.3.2 Dynamic concentration method

269 In our Grande Comore surveys, we focused on CO₂ soil emissions on the volcano flanks, where the
270 Benavente et al. (2015) surveys failed in identifying significant anomalies using the accumulation
271 chamber method. Therefore, we performed most of our measurements using the dynamic
272 concentration method in our 2017 and 2018 field works and compared them with a subset
273 acquired on the same sites using the accumulation chamber technique. This approach permits us
274 to compare the Karthala dataset with that acquired on the Piton de la Fournaise volcano (Liuzzo et
275 al., 2015). The dynamic concentration method (Gurrieri and Valenza, 1988) is based on an
276 empirically identified relationship between soil CO₂ flux and CO₂ concentration in a gas mixture
277 obtained by diluting soil gas with air (dynamic concentration), by means of a specific 50 cm probe
278 inserted into the soil. Through a constant flux rate of 0.8 l/m, the gas from the soil is pumped to an
279 IR spectrophotometer which measures CO₂ concentration. The spectrophotometer used was
280 manufactured by Edinburgh Instruments Ltd. (range 0–10%; accuracy ± 2 %; digital resolution
281 0.01%) pressure and temperature corrected and it is the same used in the surveys on Piton de la
282 Fournaise volcano. The CO₂ flux is derived from the CO₂ dynamic concentration value through an
283 empirical relationship (2) verified experimentally in the laboratory for a range of applicable
284 permeability 0.36–123 μm^2 and pumping flux 0.4–4.0 L/min:

$$285 \quad \text{CO}_2 = (32 - 5.8 \cdot k^{0.24}) C_d + 6.3 \cdot k^{0.6} \cdot C_d^3 \quad (4)$$

286 where ϕCO_2 is the soil CO₂ flux expressed in kg m⁻² d⁻¹, k is the numerical values of the gas
287 permeability (μm^2), and C_d is the numerical value of molar fraction of the diluted CO₂
288 concentration. In this work, ϕCO_2 is converted into g m⁻² d⁻¹. For more details on the method, see
289 Camarda et al. [2006a, 2006b]. In this work we used a k value of 30, which is very close to the k
290 value (35) used at Reunion island in previous studies on Piton de la Fournaise (Boudoire *et al.*,
291 2017; Liuzzo *et al.*, 2013; Liuzzo et al., 2015). In consideration of the typical range of permeability
292 in volcanic soils, k=30 value is a reasonable value limiting the error into less than 7% of the
293 measurement (see table S1 supplementary materials).

294 4. Results

295 4.1 Gas composition of fumaroles and bubbling gases

296 4.1.1 Chemistry

297 Karthala gases (CC, from the summit caldera fumaroles; LS from the Soufrière area. For the
298 locations see figure 5 and 6) show a general higher degree of air contamination with respect to
299 Mayotte samples (table 3), with the exception of sample Ka-Su-01 from Soufrière that shows the
300 highest CO₂ concentration (up to 92.2%), a significant content of H₂ (25,992 ppm), low
301 concentrations of CH₄ (346 ppm). With regard to noble gases, He varies in a narrow concentration
302 range (10.0-12.7 ppm), ²⁰Ne is between 0.03 (sample Ka-Su-01) and 7.7 ppm, ⁴⁰Ar 32.8 (sample Ka-
303 Su-01) and 5,152.8 ppm. In the Mayotte sample set noble gases show a variable concentration,
304 with He ranging between 8.2 and 113.2 ppm, ²⁰Ne between 0.052 and 7.65 ppm, ⁴⁰Ar in the range
305 55.1-3346.6 ppm. Among the other samples taken from high flux pools, only the sample CI-1a has
306 a significant air contamination, showing concentrations of N₂ and O₂ of 54.9% and 14.9%
307 respectively. The BAS bubbling gases from the tidal flat show a CO₂ dominant composition up to
308 98.69% and a variable concentration in CH₄ ranging between 416 and 2982ppm. The concentration
309 of CH₄ increases significantly in the “MAN” samples, taken from low-flux pools located close to
310 littoral mangroves (up to 4621 ppm). In the BAS samples, H₂ and CO are generally in low
311 concentrations ranging between 2.2 and 318 ppm for H₂ and 0.7 and 18 ppm for CO.

312 The chemical composition of Karthala and Mayotte gases is plotted in the ternary diagrams of
313 Figure 2. The relative proportions of N₂, He and Ar, display a mixing trend between a He-rich
314 component and a atmospheric component (air or air-saturated water – ASW). Both gases from the
315 fumarolic Karthala areas (CC and LS) and the bubbling gases from Mayotte (BAS) show a variable
316 degree of contamination by an atmospheric endmember, and its contribution is higher for air than
317 for ASW. On the whole, the He-Ar-N₂ variability falls within a typical compositional range of crustal
318 gases of which the two dominant mixing sources appear to be atmospheric and MORB-type
319 mantle, well distinguished from typical subduction-related gases. An exception is the sample Ka-
320 Su-01 which is significantly different from the present Karthala database, where only the samples
321 SKM182 and SKM183 (fumarole 6 - survey 2014 Benavente et al. 2015) show some similarity in
322 low ⁴⁰Ar and He/N₂ ratio. The chemical composition in relation to the plot of CO₂-CH₄-He highlights
323 that low temperature gas seeps of Mayotte have a larger CH₄ proportion with respect to Karthala
324 fumarolic gases. In the plot, it is also reported the field of variability of La Reunion bubbling gases
325 that allows to argue that Comoros gases are in general CH₄-enriched.

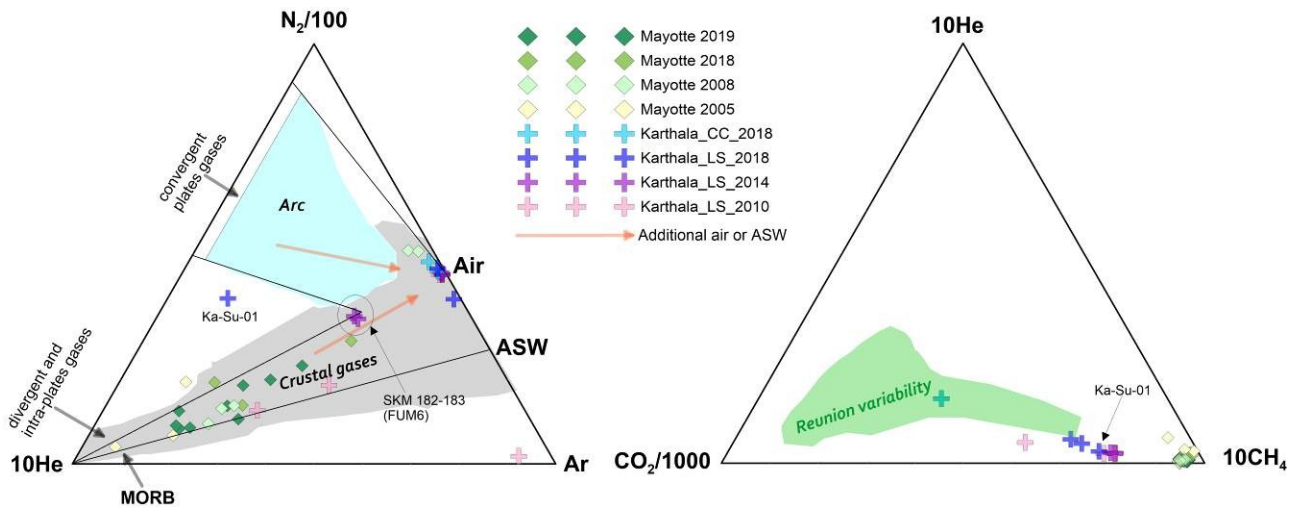


Figure 2. Relative proportion of He-Ar-N₂ in a ternary diagram on the left showing also the areas of crustal gases and arc volcanism from literature. Data collected at Grande Comore and Mayotte show a variable air and ASW contamination. CO₂-CH₄-He ternary diagram on the right displays a relatively CH₄-enrichment of Grande Comore and particularly in Mayotte. For comparison is also shown the field of variability of La Reunion gases.

4.1.2 Isotopic ratios of noble gases, CO₂ and CH₄

Table 1 reports the isotopic compositions of noble gases CO₂, and CH₄ of the sampled gases.

Karthala gases have R/Ra values ranging from 3.8 (Ka-Su-02) and 5.71 Ra (Ka-Su-01), with an overlap between CC and LS emissions. After correction for the contamination by atmospheric fluids (Rc/Ra), the highest ³He/⁴He value (5.72) is still measured in the sample Ka-Su-01, since it has the minor air contamination. Instead, the other samples range from 5.4 to 5.9 Ra due to a variable atmospheric contribution. In gases from Karthala, the ⁴He/⁴⁰Ar* ratio calculated after the correction of ⁴⁰Ar for atmospheric contamination (see eq. 2 in section 3.2) is available only for sample Ka-Su-01 and is 1.4. The relatively higher air contamination in Karthala gases, than in Mayotte gases, is also highlighted by the ⁴He/²⁰Ne (⁴He/²⁰Ne_{air}=0.318), which is generally low with an average of 1.5 (with exception of Ka-Su-01, ⁴He/²⁰Ne = 356.58), and ⁴⁰Ar/³⁶Ar (⁴⁰Ar/³⁶Ar_{air}=295.5), which is in average 303.2 (with exception of Ka-Su-01, ⁴⁰Ar/³⁶Ar = 378).

In the BAS bubbling gases there is the lack of a strong air contamination as previously indicated by the chemistry of these gases since the ⁴He/²⁰Ne ratios (up to 1663) are orders of magnitude higher the ratio in air (0,318), therefore no significant changes can be observed in the comparison between R/Ra and Rc/Ra values, except for only one sample (MAR-1) sampled in 2018. In fact, this sample shows a ³He/⁴He ratio of 3.2 Ra and a ³He/⁴He ratio of 4.2 (Rc/Ra) after correction for air contamination. The latter value strongly differs from the rest of the dataset of BAS gases, thus we suspect that this sample underwent some storage and transport to the laboratory issues that

fractionated the $^3\text{He}/^4\text{He}$, leading us to exclude it for the following discussion. In support of this, we highlight that the sample MAR-3 collected in April 2019 from the same degassing area yielded an Rc/Ra value of 7.2 (Table 3). The $^4\text{He}/^{40}\text{Ar}^*$ values of BAS gases range between 1.2 and 1.7 with a general overlap of the values among the different emissions and surveys. $^4\text{He}/^{20}\text{Ne}$ in Mayotte samples vary up to 1660 and only the MAR-1 and MAN-2 ($^4\text{He}/^{20}\text{Ne} = 1.07$ and 43.59, respectively) samples, both taken from pools with a relatively low flux, show significant air contamination. The variability of $^{40}\text{Ar}/^{36}\text{Ar}$ span up to 434, with MAR-1 and MAN-2 again showing the highest air contamination ($^{40}\text{Ar}/^{36}\text{Ar} = 290$ and 308, respectively). The C-isotope composition of CO_2 ($\delta^{13}\text{C}_{\text{CO}_2}$) of Karthala gases varies between -4.98‰ and -4.48‰ , except for sample Ka-Su-02 that shows the most positive value of -3.91‰ . At Mayotte the $\delta^{13}\text{C}_{\text{CO}_2}$ values of BAS gases vary from -5.74‰ and -3.5‰ , whereas the most negative ratios are measured in samples from MAN. The C and H pair isotope in methane were measured only in BAS gases. In detail, the C-isotope composition of CH_4 ($\delta^{13}\text{C}_{\text{CH}_4}$) was determined in most of the samples and varies between -24.4‰ and -18.7‰ , except for two samples from MAN 1 and 2 that showed the less negative ratios of -12.4‰ and -11.7‰ . The H_2 -isotope composition of CH_4 ($\delta\text{D}_{\text{CH}_4}$) was measured only in C1-2 and DIST-1 that were sampled in 2019 through Giggenbach bottles to enrich the concentration of CH_4 of dry gases. These samples yielded a δD of -118.1‰ and -137.8‰ V-SMOW, respectively.

5. Discussion

5.1 Light noble gas signature

Our new He-isotopic data for Karthala and Mayotte span a significant range of $^3\text{He}/^4\text{He}$ signatures ($4.18\text{--}7.53$ Ra), with systematic differences between the two islands of Comoros archipelago. In detail, gases from Mayotte show Rc/Ra values higher than those from Karthala. Interestingly, the Rc/Ra variability we measured in 2017-2020 gases from Mayotte ($7.5\text{--}6.4$ Ra) and Karthala ($5.9\text{--}4.7$ Ra) matches that found in fluid inclusions from the two active volcanic edifices of the Grande Comore, la Grille and the Karthala (6.9 and 5.2 Ra respectively; Class et al., 2005). In Figure 3, we modelled two air-magma mixing curves considering data from Class et al. (2005) at Grande Comore and considering the average of the values for La Grille and Karthala fluid inclusions as representative of possible mantle reservoirs end-members. According to Class et al. (1998, 2005, 2009) that propose the presence of a plume contribution in the mantle beneath Gran Comore, our data show that Comoros gases have a low-He signature, like the fluid inclusions in lavas from the

383 same volcanic systems (Karthala volcano). This low $^3\text{He}/^4\text{He}$ signature is well distinct from that
384 documented in typical hot-spot contexts like the adjacent Afar region (R/R_a up to 19.6; Marty et
385 al., 1996; Hilton et al., 2011) and la Réunion ($R/R_a = 14.5\text{--}12$; Marty et al., 1993; Boudoire et al.,
386 2020). In Figure 3, data of bubbling gases of Piton des Neiges from La Reunion are plotted together
387 with two mixing curves that explain their variability, showing that they fall within the range of $R_c/$
388 R_a values measured in fluid inclusions of eruptive products of the island.

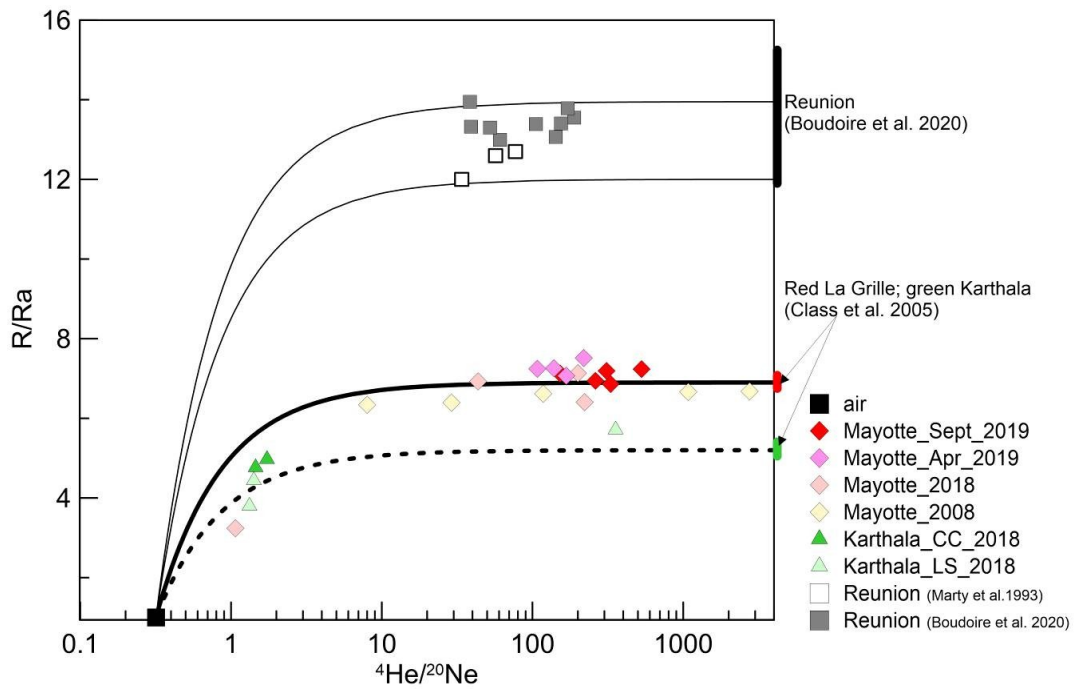
389 Ocean island basalts (OIB) from the Comoros archipelago display geochemical features different
390 from the other Indian OIB [Späth et al. (1996), Class and Goldstein (1997), Class et al. (1998),
391 Claude-Ivanaj et al. (1998), Deniel (1998), Class et al. (2009), Pelleter et al. (2014), Bachelery and
392 Hemond (2016)]. Comoros volcanisms has produced a suite of variably silica-undersaturated,
393 alkaline lavas (from melilitites and basanites, to alkali basalts to phonolites), enriched in
394 incompatible trace elements and with variable relative depletion in K. With the exception of La
395 Grille lavas, most lavas on the Archipelago record the signature of variable degrees of fractionation
396 during their storage and ascent to the surface after their emission from the deep garnet-bearing
397 mantle source (Bachelery et al., 2016). Several geochemical models have been proposed to explain
398 the elongated array of their Sr-Nd-Pb isotopic signature, whose end-members range from i) mixing
399 between heterogeneous deep plume sources (EMI, HIMU) and a shallower depleted convective
400 ambient mantle or ii) mixing between a homogeneous deep plume sources (EMI component), plus
401 a variable contribution of the shallower heterogeneous and old metasomatised oceanic
402 lithosphere. Whatever the source of the mantle heterogeneities, all authors agree that Karthala
403 lavas and rare old samples from Mayotte record the strongest EM1 contribution of the Comorian
404 plume (Pelleter et al., 2014). According to Class et al. (1998), the alkali basalts of Karthala reflect
405 mainly plume derived melts, while the basanites of La Grille are the products of interaction of
406 plume melts with the metasomatised oceanic lithosphere. Class et al. (2005) show that olivines in
407 Grande Comore lavas span a relatively small range of low- $^3\text{He}/^4\text{He}$ compositions. La Grille
408 “lithosphere-dominated” lavas have preserved a nearly MORB signature ($6.75\text{--}7.08 R_A$) suggesting
409 that amphibole forming metasomatism occurred before the arrival of the plume. All samples show
410 good correlations between Sr-Nd-He isotope ratios, indicating that the Grande Comore $^3\text{He}/^4\text{He}$
411 ratios are not significantly influenced by crustal contamination and reflect recent mixing between
412 plume- and lithosphere-derived melts. These authors highlight that the deep plume component
413 has a low and well constrained $^3\text{He}/^4\text{He}$ signature of $5.2 \pm 0.2 R_A$. On the basis of the correlation
414 with Osmium isotopes, Class et al. (2009) argue that the low-He signature does not record

415 contribution from subcontinental lithospheric mantle, but that of a deep plume interacting with
416 oceanic lithosphere. In this frame, the Comoros plume would represent a “low $^3\text{He}/^4\text{He}$ – high
417 $^{187}\text{Os}/^{186}\text{Os}$ ” hotspot whose deep source is dominated by recycled ^4He -rich material.

418 A detailed treatment of this topic is out of the scope of this paper and will be treated in ongoing
419 studies. Whatever the specific process producing the low- $^3\text{He}/^4\text{He}$ signature, we show that
420 Karthala gases record a signature consistent with that recorded in the fluid inclusions of its lavas.
421 On the contrary, Mayotte gases have a slightly higher $^3\text{He}/^4\text{He}$ signature, which matches that of la
422 Grille lavas. These findings are consistent with the barometric results of previous works (Bachèlery
423 et al., 2019; Berthod et al., 2020) on the lavas of Mayotte submarine eruption, showing that these
424 evolved basanite magmas are extracted by large shallow mantle reservoirs (50-20 km depth)
425 located between the Moho and the upper oceanic lithosphere.

426 The $^4\text{He}/^{40}\text{Ar}^*$ values measured in Karthala (only one reliable value) and Mayotte gases vary in a
427 narrow range (1.2-1.7), falling within that typical of fertile mantle ($^4\text{He}/^{40}\text{Ar}^* = 1-5$; Marty, 2012)
428 and magmatic values from other geodynamic settings (e.g., Paonita et al., 2012; Bräuer et al.,
429 2013; Boudoire et al., 2018; Rizzo et al., 2019). In magmatic environments, this ratio varies during
430 melts degassing and is indicative of relative entrapment pressures (e.g., Paonita et al., 2012;
431 Boudoire et al., 2018). Focusing on Mayotte gases for which $^4\text{He}/^{40}\text{Ar}^*$ is available for different gas
432 emissions and surveys dates, we do not notice systematic variations. This leads us to two
433 important deductions: the first is that this ratio is not modified by gas-water interaction as e.g. $\text{He}/$
434 CO_2 (see section 5.2) and thus can be used to track temporal variations eventually related to
435 changes in magmatic dynamics; the second is that Mayotte gas emissions reflect a magmatic
436 degassing occurring in a narrow range of depth. In other words, we could consider a
437 homogeneous (in terms of depth) source of degassing. If we consider the findings of a recent study
438 carried out at La Reunion, in which Boudoire et al. (2018) constrained a range of $^4\text{He}/^{40}\text{Ar}^* = 2.1 \pm 0.4$
439 for fluids exsolved at underplating (10-15 km below Piton de la Fournaise), assuming a comparable
440 ratio in primary magmas below Mayotte, we could speculate that BAS emissions reflect the
441 degassing of a melt ponding at comparable depths. Finally, the lack of evident temporal variations
442 leads us to consider limited depth variations of the melt feeding the discharge of BAS emissions.

443



444

445 Figure 3. $^4\text{He}/^{20}\text{Ne}$ versus $^3\text{He}/^4\text{He}$ (R/Ra) in fumaroles and bubbling gas from Grande Comore and Mayotte. For
 446 comparison are shown data from bubbling gases at La Reunion from Bouidoire et al., (2020) and Marty et al., (1993).
 447 Thick and dash black lines indicating air-magma mixing are calculated from the average value [from Class et al.,
 448 (2005)] of La Grille and Karthala fluid inclusions respectively. Thin black lines are calculated as the minimum and
 449 maximum of bubbling gases at La Reunion. At the right side of the diagram are also indicated three solid black red and
 450 green bars, corresponding to the range of the R/Ra variability of La Reunion, La Grille and Karthala fluid inclusions
 451 respectively.

452

453 5.2 Evidences of gas-water interaction and origin of CO_2 and CH_4

454 To evaluate the carbon origin of CO_2 in Karthala and Mayotte gases, $\delta^{13}\text{C}$ is diagnostic of the
 455 original geochemical environment, being able to discriminate between a magmatic source ($-$
 456 $8\text{‰} < \delta^{13}\text{C} < -4\text{‰}$; Sano and Marty, 1995), the contribution from subducted marine limestone with
 457 $\delta^{13}\text{C} = 0\text{‰}$, and sedimentary rocks of organic origin with much lighter $\delta^{13}\text{C} = -25\text{‰}$ (Hoefs, 2015).
 458 Thus, we correlated the variation of the $\text{CO}_2/{}^3\text{He}$ versus $\delta^{13}\text{C}$ ratio based on the approach proposed
 459 by Sano and Marty (1995 and references therein). Figure 4A plots two mixing curves modelled
 460 considering both an organic and a limestone endmember, in which the mantle corresponds to
 461 $\text{CO}_2/{}^3\text{He} = 5.0 \times 10^9$ and $\delta^{13}\text{C} = -4.4\text{‰}$, which result from the average values of our data and data from
 462 literature. For both organic and limestone endmembers, a value of $\text{CO}_2/{}^3\text{He} = 1.0 \times 10^{13}$ is assumed,
 463 whereas for organic and limestone $\delta^{13}\text{C}$ endmember is assumed $\delta^{13}\text{C} = -25\text{‰}$ and $\delta^{13}\text{C} = 0\text{‰}$
 464 respectively (Sano and Marty, 1995). As known from other studies in hydrothermal gases (Capasso
 465 et al., 2005; Gilfillan et al., 2009; Dubaqc et al., 2012; Rizzo et al., 2019), the $\text{CO}_2/{}^3\text{He}$, He/CO_2 , $\text{CH}_4/$
 466 CO_2 ratios and $\delta^{13}\text{C}$ isotopic signature can be potentially modified by gas-water interaction in

which CO₂ dissolves preferentially with respect to the other species. These effects need to be evaluated and eventually filtered out in order to calculate the thermobarometric conditions of the hydrothermal system feeding the gas seeps (Figures 2 and 4). In Mayotte gases, we observe only a modest variability of the He/CO₂ ratio (Figure 4), which overlaps with that found in Karthala fluids, with the exception of two 2018 samples from the “MAN” pools with low gas flux that show He/CO₂>1.0x10⁻⁴. Similar evidences were observed by BRGM in 2005 samples 9a,b,c over the whole Mayotte tidal flat (Traineau, 2006) and might suggest an increase in gas fluxes after 2005. In order to constrain the pristine C isotopic signature of CO₂ in Karthala and Mayotte, we modelled a Rayleigh fractionation assuming a dissolution under equilibrium conditions based on the approach used in Rizzo et al. (2019). The Clark and Fritz (1997) equation is as follows:

$$\delta^{13}C_{CO_2} = \epsilon + \ln f \quad (5)$$

where the subscript 0 indicates the initial CO₂ isotope composition and f is the fraction of the residual gas phase, while ϵ is the fractionation factor between DIC (dissolved inorganic carbon) and gaseous CO₂ (CO_{2(g)}). In turn, ϵ depends on water temperature and pH, which are unknown, therefore, for our purpose the values of temperature and pH has been chosen which better approximate our dataset corresponding to T=32°C and pH=5.71. These values correspond to those measured in the marine water of the Mayotte tidal flat by BRGM surveys (Traineau, 2006; Sanjouan, 2008). Our results show that Karthala gases are not evidently affected by interaction with shallow waters, as well as most Mayotte bubbling gases record only a minor partial dissolution of CO₂ (Figure S1 supplementary materials). The modest effect of preferential dissolution of CO₂ in water with respect to CH₄ and He is evident in Figure 4B, where He/CO₂ vs Rc/Ra are shown. Therefore, not considering the samples MAN affected by minor dissolution effects, the general variability of Mayotte and Karthala gases falls well within the range of mantle values (Figure 4A). In spite of streaming through a thick carbonate sequence of the coral reef or of the extensive bacterial contribution recorded in the nearby gas bubbling of the Dziani lake (Milesi et al., 2019, 2020), the gases of Mayotte tidal flat do not show any obvious limestone or organic contributions. Their magmatic signature can be constrained at $\delta^{13}C \approx -4.3\text{‰}$, which can also represent the magmatic signature of Karthala gases. This statement is supported by the narrow variability of $\delta^{13}C$ range both at Karthala fumaroles ($-4.9\text{‰} \leq \delta^{13}C \leq -3.9\text{‰}$) and Mayotte BAS high flux bubbling pools least affected by gas-water interaction ($-4.9\text{‰} \leq \delta^{13}C \leq -3.5\text{‰}$), as well as by their relatively stability in time considering data from BRGM of 2006 and 2008 campaigns ($-4.3\text{‰} \leq \delta^{13}C \leq -$

3.2‰) as well as in 2016 with $\delta^{13}\text{C} = -3.2\text{‰}$ (G7 point by Milesi et al., 2020). Therefore, a $\delta^{13}\text{C} \approx -4.3 \pm 0.2\text{‰}$ is a reasonable approximation of a possible $\delta^{13}\text{C}$ magmatic signature for the Archipelago.

If compared to the bubbling springs of La Réunion (Figure 4A), we notice that the $\delta^{13}\text{C}$ signature of Mayotte and Karthala gases is slightly less negative and shows a minor variability. It is worth noting that La Réunion gases with $\delta^{13}\text{C} \approx -6\text{‰}$ display a trend of decrease of $\text{CO}_2/{}^3\text{He}$ suggesting the occurrence of a process of selective dissolution of CO_2 in water, which is observed in Mayotte only for the samples MAN 1 and 2.

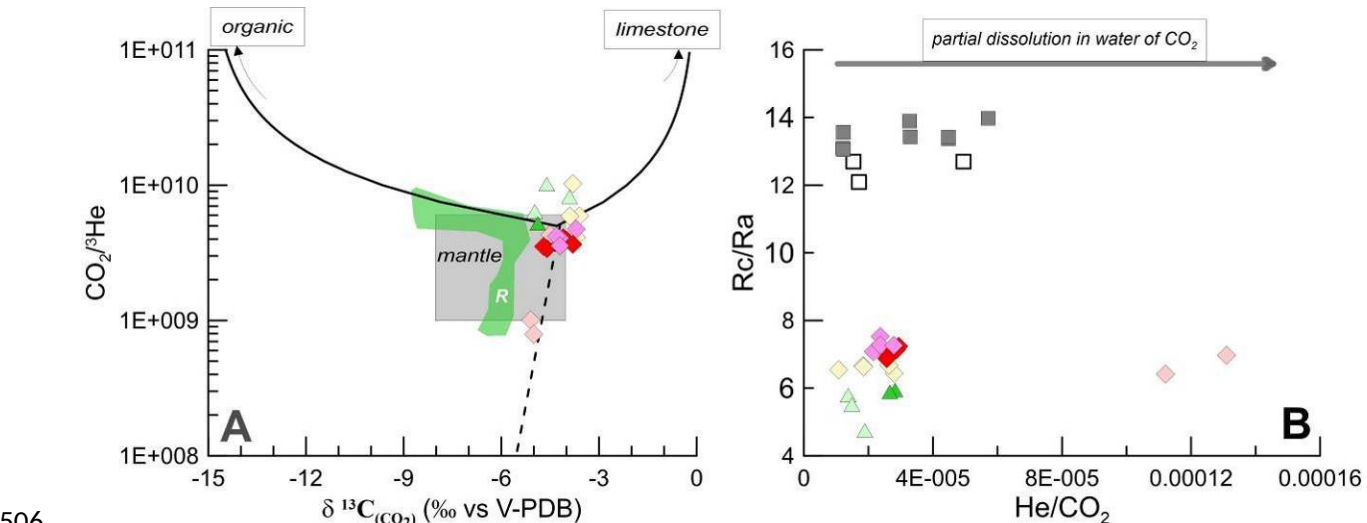


Figure 4. A: $\delta^{13}\text{C}$ of CO_2 versus $\text{CO}_2/{}^3\text{He}$ diagram of fumaroles and bubbling gases at Grande Comore and Mayotte. B: He/CO_2 versus Rc/Ra . Symbols as in figure 3. For comparison is indicated also the variability of corresponding gases at La Reunion (R). Diagram 4A shows that gases at Comore archipelago are in the field of Mantle-like origin with no evident organic or limestone contributions. Solid lines are mixing curves between organic, mantle and limestone endmembers, while the dashed line indicates a Rayleigh fractionation dissolution. Diagram 4B displays a variable degree of water-gas interaction affecting CO_2 variability.

Even if the Karthala and Mayotte fluids are CO_2 dominated, we recall that they show a progressive enrichment in CH_4 up to concentrations of 2982 ppm in gases from Mayotte, which allowed to measure its isotopic composition of C and H (δD of methane was measured only in DIST-1 and C1-2, table 3). Following the classification proposed by Schoell (1980) (Figure S2 supplementary materials), samples DIST-1 and C1-2 could be considered of abiogenic origin, coherently with the G3 bubbling spot with the highest gas flux in the Dziani lake, recently documented by Milesi et al. (2020) The same authors report of a G7 sample in the BAS area which shows similar $\delta^{13}\text{C}$ of DIST-1 and C1-2 but very negative δD of methane (-250‰). However, it must be stressed that distinguishing between methanogenesis processes of biological origin or thermogenic processes at the origin of CH_4 (Mazzini et al, 2011; Schoell, 1980; Welhan, 1988) is complicated by possible

523 mixing between endmembers with different isotopic signature (Taran et al. 2010) or by the
524 occurrence of oxidation processes (e.g., Batista Cruz et al., 2019). It is therefore clear that further
525 data are needed to better constrain the origin of methane in the BAS area of Mayotte

526

527 5.3 CO₂ degassing from soil

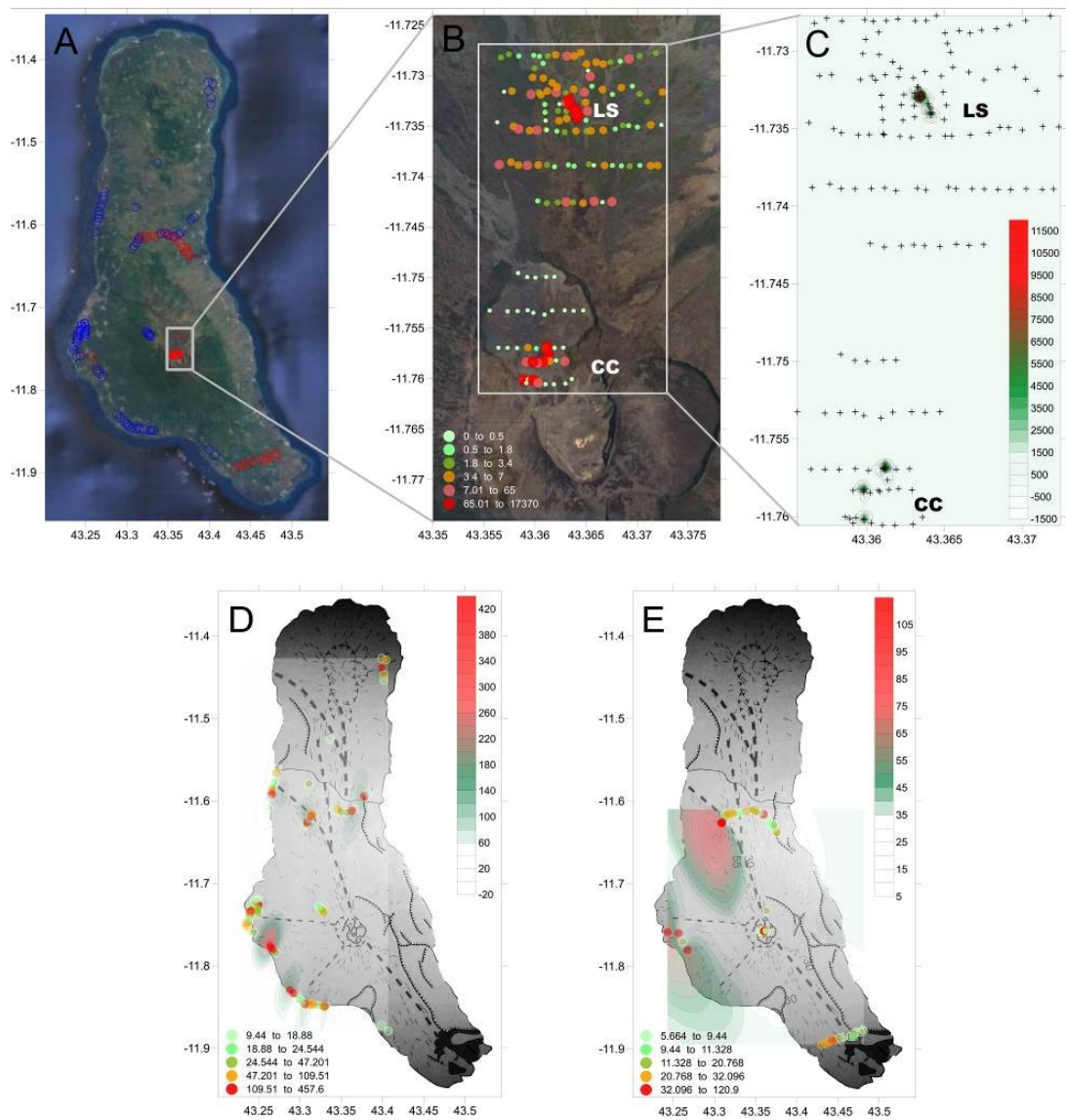
528 Volcanic areas are often places where diffuse outgassing of CO₂ emission occurs, facilitated by
529 tectonic structures which locally increase soil permeability. On seismically and volcanically active
530 areas like the Comoros, soil CO₂ emissions have been investigated in order to identify hidden
531 tectonic structures driving fluid emissions to the surface (e.g., Bonforte et al., 2013; Boudoire et
532 al., 2017; Giammanco et al., 2006; Gurrieri et al., 2008; Irwin and Barnes, 1980; Liuzzo et al., 2013).
533 In volcanic tropical settings like the Comoros, the presence of significant fraction of soil CO₂
534 emissions can also be ascribed to biogenic activity, which may be mixed with gas originating from
535 magmatic sources and whose relative proportion may evolve in time as a function of seasonal
536 effects and the evolution of the seismic and volcanic activity (e.g., Boudoire et al., 2018a; Chiodini
537 et al. 2008; Liuzzo et al., 2015).

538 While rift zones are marked by well defined alignments of volcanic cones in Grande Comore, they
539 are much less defined in Mayotte, where a set of mafic scoria cones and phonolite maars are
540 scattered on the Petite Terre island (Nehligh et al., 2013; Michon et al., 2016; Famin et al., 2020;
541 Tzevahirtzian et al., 2021). In Grande Comore, volcano flanks are often resurfaced by the frequent
542 emplacement of lava flows, nevertheless thick soils and sand covers are found in most locations,
543 suitable for the measurement of soil CO₂ fluxes. At Petite Terre, the recent explosive activity of
544 phonolitic maars emplaced a widespread cover of several meters thick fine grained ashes that,
545 together with the low altitude of the island and the widespread urban context, limit the areas
546 suitable for CO₂ flux measurements. In our survey strategy, we aimed at characterizing the CO₂
547 fluxes from the soil on the territory and linking them with known or hidden tectonic structures and
548 with the main degassing areas (summit of Karthala in Grande Comore and Dziani lake and Airport
549 tidal flat in Mayotte). Measurements on Mayotte tidal flat were performed at low tide, when the
550 sandy/muddy flat is wet but without a continuous water cover, excepted some large bubbling
551 pools. Samples of soil gas were taken alongside the soil CO₂ flux measurements to investigate the
552 isotopic signature of carbon in CO₂ and thus constrain the sources of the soil CO₂ emission. As
553 previously mentioned in 3.1, as the soil CO₂ dataset was acquired using two different methods and
554 at different times, it is not uniform and therefore our choice in data analysis was to consider each

555 area separately. Even if acquired in different seasons and times, all the measurements were
556 carried out on dry sunny days and generally stable weather conditions. Where possible,
557 measurements were performed at a spacing of ca. 50 m or less, though in some cases distances
558 between individual sites and length and orientation of the tracks were dependent upon local
559 urban density, morphological obstacles, and vegetation cover.

560 **5.3.1 Grande Comore**

561 At Grande Comore three campaigns were conducted for the measurement of soil CO₂ using two
562 different methods: a) Accumulation chamber, b) Dynamic concentration (Figure 5).



564 Figure 5. Soil CO₂ measurements at Grande Comore. In A sites of measurements distinct in blue and red for 2017 and
565 2018 surveys respectively. Inside the white rectangular are indicated the 2018 sites of measurements not indicated in
566 B. In figure 7B a classed post map of the 2014 survey at the summit of Karthala volcano realized using the
567 accumulation chamber method. CC indicates the Central Caldera area; LS indicates La Sufriere. In C a contour plot of
568 soil CO₂ emission of the Karthala summit area. Figures 7D and E are related to 2017-2018 surveys respectively realized

569 using the “Dynamic concentration method” [Gurrieri and Valenza (1988)]. On both maps it has overlapped the
570 structural map from Bachèlery and Coudray (1993).

571

572 The first survey at Grande Comore was conducted by Benavente et al. (2015) and focused on
573 exploring the potential geothermal resources of the island. Using the accumulation chamber
574 method (Chiodini et al., 1998), the survey concentrated on the summit area of Karthala volcano,
575 providing a total of 155 measurements of CO₂ flux (table 2), and only a subset of measurements
576 was performed on the volcano flanks showing very low soil degassing rates. In the summit caldera,
577 the survey by Benavente et al. (2015) focused on the northern and recently active (2007) part of
578 the caldera, consistently with previous geophysical and CO₂ surveys of Lénat et al. (1998) and
579 Bernabeu et al. (2018), showing that the strongest hydrothermal activity occurs in this area (CC
580 area). In addition, Benavente et al. (2015) provide the first dataset on the most active and high
581 temperature Soufrière area, on the northern rift (LS area). The results of the 2014 survey are
582 plotted in Figure 5 (B, C). The soil CO₂ flux ranges from background air (0 flux) up to 17,364 g/
583 m²day. The grid of points in the area investigated by Benavente et al. (2015), was suitable for the
584 estimation of the total budget of CO₂ flux emission at that period, resulting in an average of 288.8
585 and 559.5 g/m²day at the crater and La Soufrière areas respectively. The remaining summit area
586 investigated of Karthala volcano is characterized by a general very low average of CO₂ flux.

587 In 2017 and 2018, the second and the third soil CO₂ measurement surveys were carried out by
588 IPGP and INGV teams, using the Dynamic method (Gurrieri and Valenza, 1988) and focusing on the
589 volcano flanks and La Grille area. The unknown *k* value, necessary for the application of the
590 dynamic method (equation 2), has been chosen from those which give the minimum percentage
591 deviation between the most probable range of *k* values in volcanic soils (Camarda et al., 2006a)
592 and in consideration of the similarity with soil CO₂ emission measured at La Reunion (Boudoire et
593 al., 2017; Liuzzo et al., 2015). For all the measurements at Karthala a *k* value of 30 μm² has been
594 chosen (see supplementary materials Table, S2). Considering reasonable that the probable range
595 of permeability in volcanic soil ranges between 20 and 40 μm², the percentage deviation is less
596 than 6.5% in all the measurements carried out at Karthala.

597 87 measurements were taken during the 2017 campaign in the distal area of the Karthala volcano
598 (table 1), with soil CO₂ flux ranging between approximately 9 and 450 g/m²day (table 2). During the
599 2018 campaign, we carried out 65 measurements, where some were partially overlapping the
600 previously surveyed area, however most were in new areas not covered by the 2017 survey

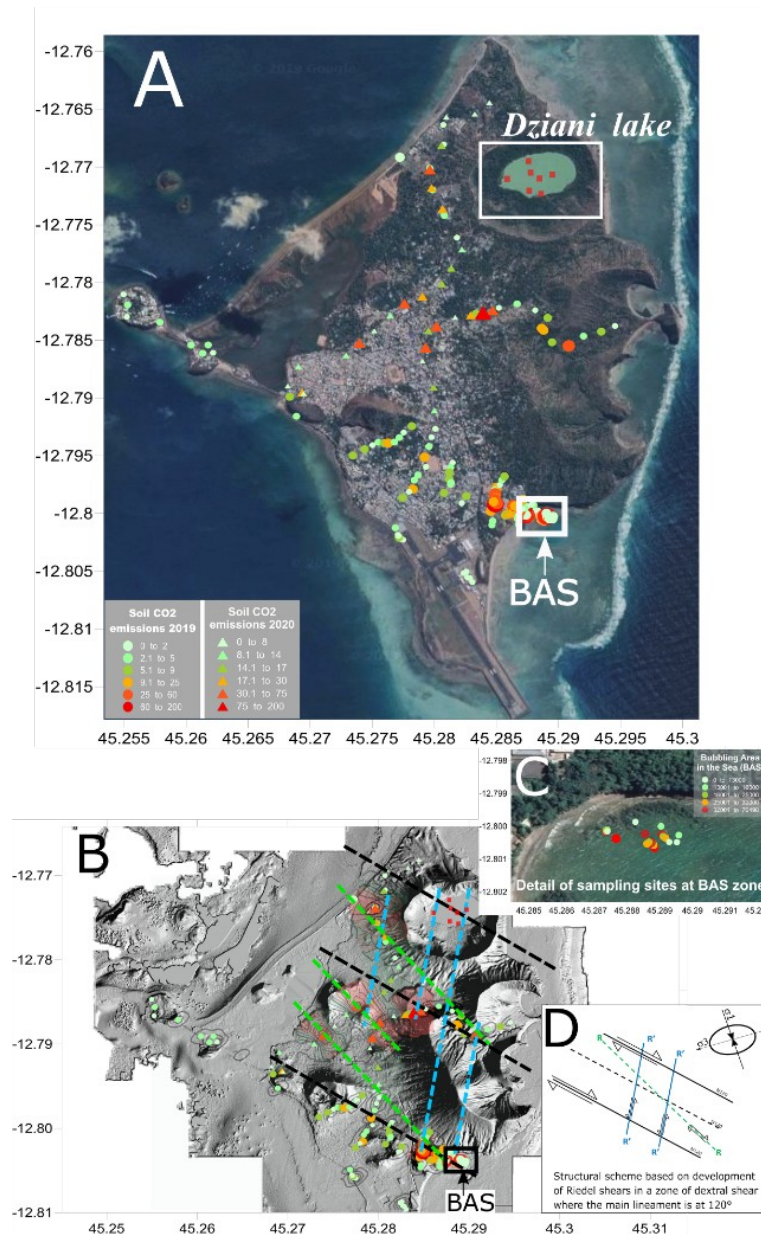
601 (Figure 7A). In 2018, minimum and maximum fluxes are around 5 and 950 g/m²day respectively,
602 and confirmed that the maximum fluxes occur inside the summit caldera, close to the CC hot
603 ground and fumarolic field. The findings of these two campaigns (Figure 5D and 5E) show a clear
604 correlation between the main structures (Bachelery and Coudray, 1993) and the highest flux
605 emissions, confirming that the spatial distribution of the soil CO₂ flux is tightly linked to the
606 tectonic structures of Grande Comore. The Soufrière fumaroles and the maxima on the volcano
607 flank fall on the main rift zones previously identified on the basis of the alignment of volcanic
608 cone. Interestingly, anomalous areas of high CO₂ soil flux extend at low altitude, both in the
609 northern and western part, where a recent seismic and volcanic activity has occurred, while very
610 low fluxes are measured in the southern part of the island, which corresponds to the oldest little
611 active part of Grande Comore (see Bachelery et al., 2016 for a recent review).

612 Soil gas fluxes and their spatial distribution reminds that documented on Piton de la Fournaise
613 volcano where fluxes, in the range 5.52 to 701.56 g/m²day, have been measured during
614 quiescence phases (Liuzzo et al., 2015). In spite of its strong eruption rate, Piton de la Fournaise
615 lacks an area of strong degassing near its summit, which instead occurs on the older and quiescent
616 Piton des Neiges volcano (Marty et al., 1993; Boudoire et al., 2020).

617 5.3.2 Mayotte - Petite Terre

618 The occurrence of a widespread ash cover makes the dynamic concentration method not suitable
619 for most CO₂ flux measurements at Petite Terre, Mayotte, where surveys were performed using
620 the accumulation chamber method in September 2019 and in November 2020 (Figure 6). On this
621 island, a total of 166 measurements of CO₂ flux were taken from the soil and 53 on the tidal flat of
622 the Airport (BAS: bubbling area in the sea Figure 6C). We did not perform a CO₂ survey inside the
623 Dziani crater, however it represents a target of future investigations. Not surprisingly the strongest
624 CO₂ soil emissions were measured in the Airport tidal flat, where the CO₂-rich bubbling pools are
625 located, with a range of values between 12 and 70,485 g/m²day. Peak emissions are thus 4 times
626 higher than those measured at Karthala. The grid of points for this initial exploration did not lend
627 itself to estimating the overall CO₂ flux budget, which will instead be the focus of future
628 investigations. On land, we measured fluxes that span from background levels (corresponding to
629 the air values concentrations) to 173.4 g/m²day, being much lower than in the volcano flanks of
630 Karthala or of la Réunion. Our surveys show that at Mayotte the underlying hydrothermal system
631 is the main source of the outgassing of the island and the bubbling area on the tidal flat is an
632 important area of high CO₂ flux. This could arise from a combination of high fluxes focused in two

633 areas (Airport tidal flat and Dziani) and the widespread and poorly permeable fine ash cover on
634 Petite Terre. The possible influence of the ash cover on soil CO₂ fluxes is however not
635 straightforward. At Petite Terre, the thickness of fine ashes increases from west to east and the
636 soil CO₂ fluxes as well, together with the occurrence of the two main areas of gas bubbling, which
637 are located on the eastern side of the island. Even if the on land soil CO₂ emissions are generally
638 modest compared with other sites, their spatial distribution still permits to identify preferential
639 areas of CO₂ emissions on the ground and to discuss their possible link with hidden tectonic
640 structures, not always recognisable with other methods of investigation. Available datasets
641 (Tzevahirtzian et al., 2021; Famin et al., 2020) show that Petite Terre is the tip of a huge and
642 mostly submarine volcanic ridge with a broad regional alignment in the N120° direction,
643 corresponding to the main regional structure of Comoros archipelago and interpreted as a right-
644 lateral shear in the lithosphere (Famin et al., 2020; Michon, 2016). Results from our surveys
645 (Figure 6B) show a distribution of soil CO₂ degassing which might be overlapped to a possible
646 structural scheme in which a system of fractures is determined by a combination of the main
647 structural trends along N120° and a combination of Riedel's structures coherent with the right
648 shear (Figure 6D). In this scheme, the N120° is well correlated to the alignment of Holocene
649 tephritic scoria cones corresponding to the oldest phase of the recent volcanism of Petite Terre
650 (Nehilg et al., 2013). A NNE-SSW (R') trend of soil CO₂ emission is overlapped on the most recent
651 volcanism of the phonolitic maars, where the principal evidence of outgassing is shown by the BAS
652 zone at the feet of the large "Vigie" maar and the bubbling manifestation inside the Dziani lake
653 (Milesi et al., 2020). A possible trend corresponding to R structures is also appreciable in the
654 central area of the island. Even if this first approach proposes an interpretative evaluation of the
655 spatial outgassing distribution, however it must be stressed that future investigations on larger
656 areas are needed to better understand the detailed structural pattern on Mayotte Island.



657

658 Figure 6. (A) Petite Terre (Mayotte) classed post map showing 2019 and 2020 surveys indicated as circles and triangles
 659 respectively. Also shown inside the white rectangular at the Dziani lake (red squares) the bubbling area investigated by
 660 Milesi et al., (2020). BAS indicates the bubbling area in the sea, which is magnified in (C) as a classed post map of the
 661 CO₂ flux measurements carried out in 2019. In (B) digital elevation map of Petite Terre highlighting the volcanic cones
 662 and the contour map of the soil CO₂ emissions. The structural trend in (B) is adapted to the Mayotte soil emissions
 663 from the theoretical structural scheme exposed in figure (D) based on a dominant shear zone N120°.

664

665 5.4 Equilibrium temperature of hydrothermal gases

666 In the previous paragraphs, we have shown that the fumarolic and bubbling gases of Grande
 667 Comore and Mayotte have relatively high methane contents with the proportion of methane being
 668 highest at Mayotte. We also highlighted the effect on gas chemistry of partial dissolution of CO₂ in
 669 water, as well as identified the samples that showed the most evident effects of this process.

670 Data of CO₂ and CH₄ poorly or not affected by the dissolution of CO₂ in water allowed us to
671 evaluate the possible gas equilibrium conditions among different gas species in hydrothermal
672 environments. In several geothermal systems, the Fischer-Tropsch process has been successfully
673 used to define the origin of methane since the 60s (D'Amore and Panichi, 1980; Hulston and
674 McCabe, 1962). Nowadays an extensive scientific literature exists that explores the conditions of
675 equilibrium among gas species in hydrothermal environments in order to obtain useful geo-
676 indicators for temperature and pressure (Chiodini and Marini, 1998; Fischer and Chiodini, 2015).
677 Assuming that in the hydrothermal system an equilibrium is attained between the dominant
678 species H₂O-H₂-CO₂-CO-CH₄, methane can form inorganically from the reaction:



680 where the formation of methane is favoured by the decreasing temperature. For this system we
681 assumed as a condition of thermal equilibrium between CH₄ and CO₂ the equation proposed by
682 Giggenbach (1992):

683
$$\log (X_{\text{CH}_4} / X_{\text{CO}_2}) = 4625 / (t_e + 273) - 10.4 \quad (7)$$

684 where t_e is the equilibrium temperature (°C) while X_{CH_4} and X_{CO_2} are the molar fraction of CH₄ and
685 CO₂ respectively.

686 Under these assumptions, equilibrium temperatures range between around 381 and 460°C at
687 Karthala (Figures S2 supplementary m.) which is consistent with data from Benavente et al.,
688 (2015). At Mayotte temperature vary between 314 and 339 °C (excluding MAN 1 and 2 which are
689 recognized as affected by a severe dissolution of CO₂ in water). Interestingly, we do not record a
690 change neither in equilibrium temperature nor in outlet temperature (in equilibrium with sea
691 water temperature) in bubbling gases of the BAS Mayotte tidal flat in the period 2005-2019 in
692 spite of the large magmatic event occurring at ca. 50 km from its coast.

693 To explore possible evidences of recent input of deep fluids in Mayotte hydrothermal system we
694 evaluated the thermal equilibrium in combination with their isotopic signatures on the basis of
695 their $\delta^{13}\text{C}$ isotopic fractionation factor between CO₂ and CH₄. In our BAS samples, $\delta^{13}\text{C}_{\text{CH}_4}$ ranges
696 from -24.4 to -11.7‰, the most positive values corresponding to the MAN samples collected by a
697 low-flux pool close to the mangrove area (Figures S2 supplementary m.). To this aim, we have
698 combined the temperatures obtained from (7) with the temperatures (t_e) calculated using the
699 equation proposed by Bottinga (1969) valid for temperatures ranging between 0-700 °C:

$$\Delta = 22166 / (t_e + 273) - 13.8 \quad (8)$$

where Δ is the difference between $\delta^{13}\text{C}_{\text{CO}_2}$ and $\delta^{13}\text{C}_{\text{CH}_4}$ values. The relation (8) provides on the whole higher temperatures, ranging between 370 and 515°C (Figures S2 supplementary materials), where the samples MAN-1 and MAN-2 - (16-12-2018), which have been hypothesized to be affected by a strong fluid-water interaction, provide a much higher apparent equilibrium temperature up to 940°C and therefore they are not discussed further.

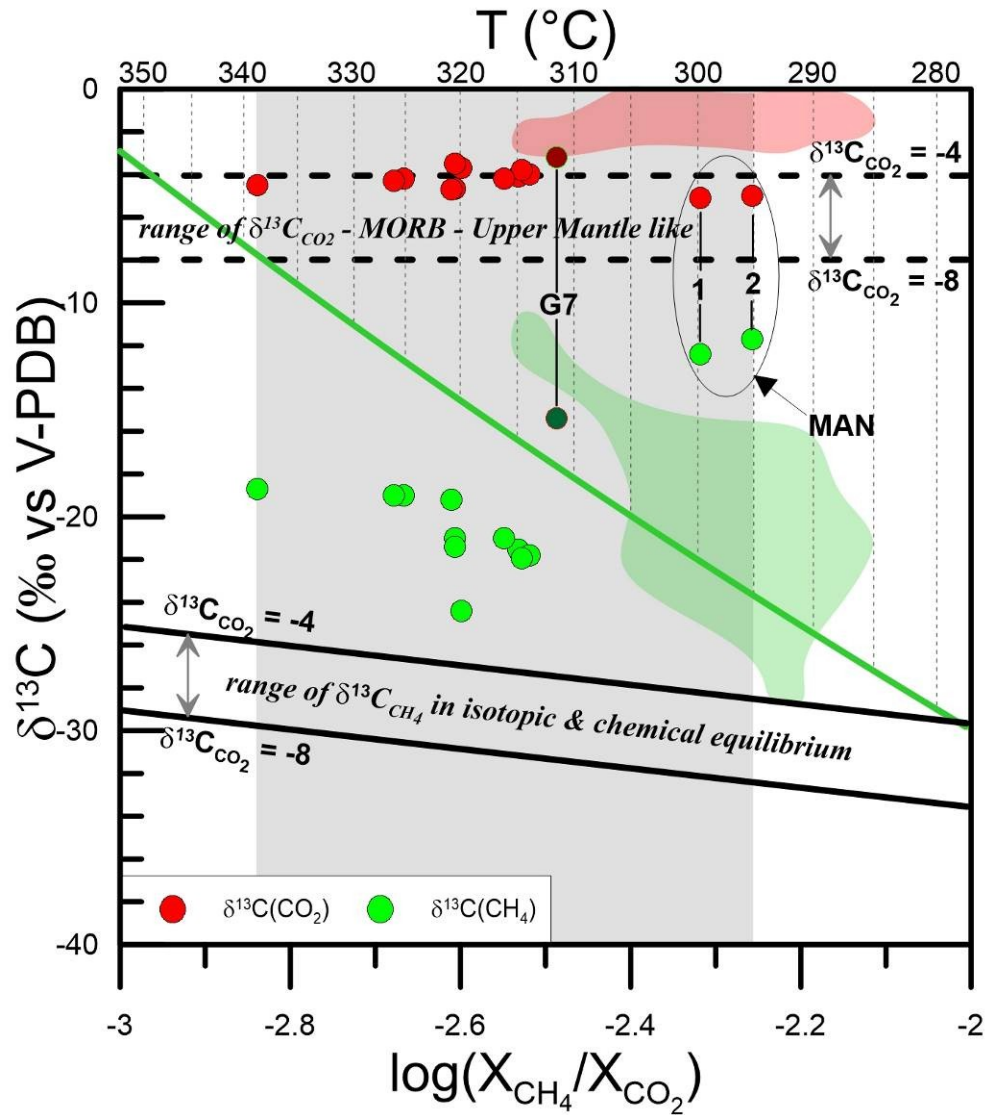
It is known that temperatures calculated from the CO_2 - CH_4 isotopic geothermometer are generally higher than temperatures obtained from geothermometers based on chemical equilibrium (Horita, 2001). This difference is attributable to several process which can affect the final equilibrium and various hypotheses have been invoked to account such outcomes. If external factors able to affect the hydrothermal system cannot be excluded (e.g. an external sources of gas interacting with the hydrothermal system) amongst the causes that might determine discrepancy on the estimation of temperature, a sort of "quenching effect" on the isotopic signature of hydrothermal gases may be considered relevant. Under this assumption, CO_2 and CH_4 were initially in isotopic equilibrium attained at the original source (supposed to be deep) however, during the ascent of the gas to shallow depths, there may not be enough time for the isotopic readjustment thus preserving the original isotope ratios. Such a quenching effect is also justifiable by the faster rate of reequilibration (about 100 times) of the chemical system than the isotopic system (Giggenbach, 1982).

In order to understand if the different temperature obtained by the chemical and isotopic geothermometers could be an expression of a quenching effect acting on the BAS area at Mayotte we plotted the log of the concentration ratio of CH_4 and CO_2 versus the $\delta^{13}\text{C}$ of both methane and CO_2 (Ono et al., 1993). In Figure 7 the thick black lines were modelled assuming that both chemical and isotopic equilibrium is maintained with a fixed $\delta^{13}\text{C}_{\text{CO}_2}$ corresponding to the range of magmatic signature, here -4‰ and -8‰ (dashed black lines) by coupling the equations (7) and (8):

$$\log \left(\frac{X_{\text{CH}_4}}{X_{\text{CO}_2}} \right) = \frac{4625(\Delta + 13.8)}{22166} - 10.4 \quad (9)$$

In addition, the equilibrium temperature calculated using the equation (7) (green line) is shown. The trend of the continuous black lines therefore should represent the variation of the $\delta^{13}\text{C}_{\text{CH}_4}$ expected if equilibrium conditions are attained by gases injected in the hydrothermal system. However, our data show a significant shift of the methane toward heavier isotopic concentrations.

730 Bacterial oxidation of thermogenic CH_4 can explain isotopic fractionation determining an increase
 731 of the isotopic ratio (Baker and Fritz, 1981; Coleman et al., 1981). For instance, this process may be
 732 probable in the Dziani lake, where Milesi et al. (2020) have underlined a probable mixing between
 733 gas of biogenic and magmatic origin.



734

735 Figure 7. $\delta^{13}\text{C}$ for CO_2 (red) and CH_4 (green) versus $\log(X_{\text{CH}_4}/X_{\text{CO}_2})$ of Mayotte bubbling gases. Dark red and green
 736 symbols are referred to the G7 sample of Milesi et al., (2020) mentioned in the text, also the red and green area are
 737 referred to the variability of the Dziani lake samples from the same authors. The green line correspond to the CH_4 and
 738 CO_2 thermal equilibrium expressed in equation (7) (Giggenbach, 1992), the thick black lines are calculated as the
 739 equation (9) for isotopic and chemical equilibrium between CH_4 and CO_2 for two cases of $\delta^{13}\text{C}(\text{CO}_2)$ corresponding at -
 740 4‰ and -8‰ which in turn are indicated as dashed lines.

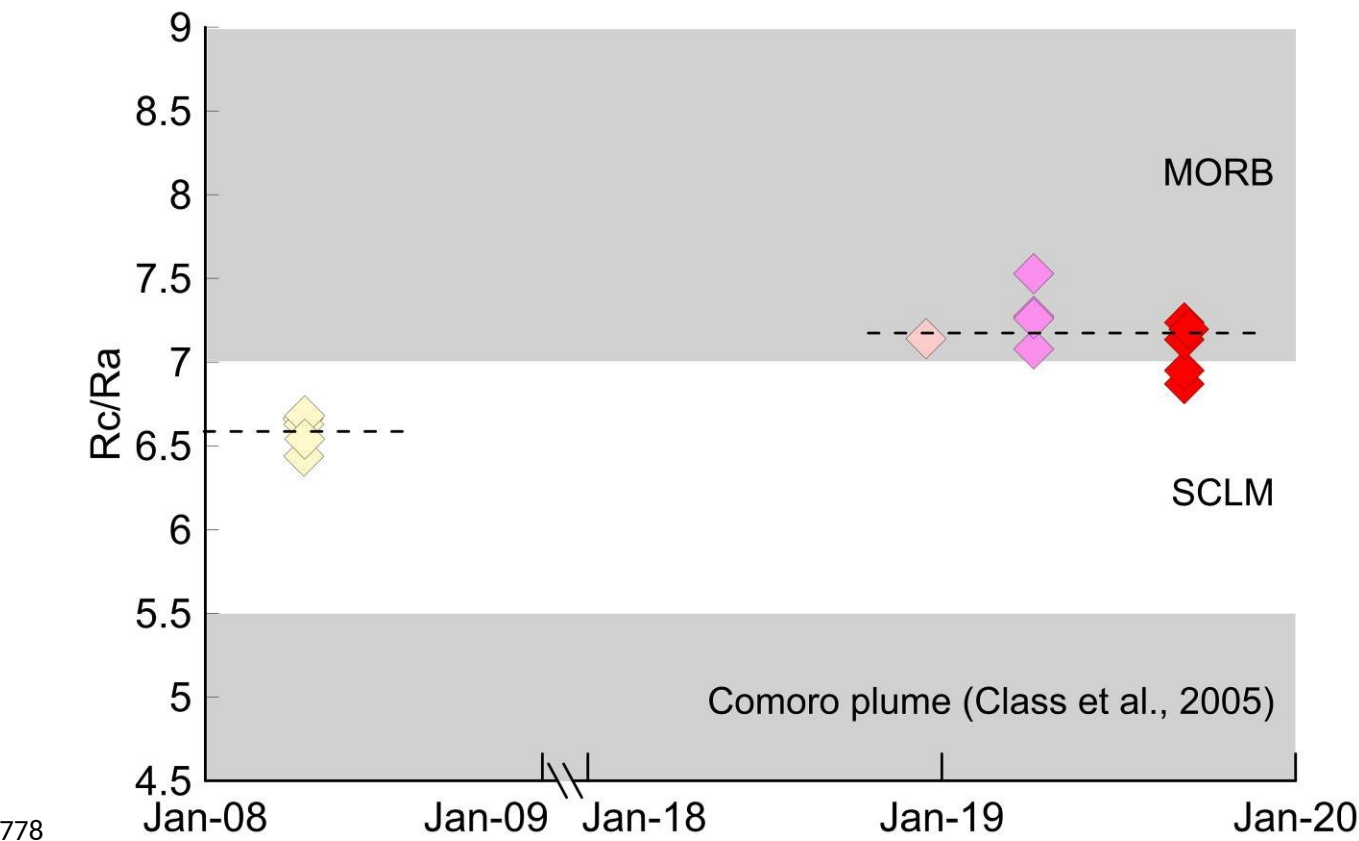
741

742 Although a carbon isotopic fractionation of methane cannot be excluded, some important
 743 differences between the gases of the BAS area and Dziani Lake should be underlined. The range of
 744 variability of $\delta^{13}\text{C}_{\text{CH}_4}$ of the BAS samples is consistent with an abiogenic source (Schoell, 1980).

Moreover, the δD values of the samples DIST -1 and C1-2 are -137.8‰ and -118.05‰, respectively, being much higher than the value of G2 (-272‰) methane-rich pool of Dziani lake reported by Milesi et al. (2020), confirming a probable abiotic origin of methane at BAS. Chemical equilibrium temperatures are systematically higher at BAS than at Dziani (<290°C), further suggesting an inorganic origin of BAS methane, or a more magmatic contribution in the hypothesis of a binary mixing between biotic and abiogenic methane. The methane-rich geochemical environment of the Dziani gases is definitely conditioned by the microbial activity in lacustrine waters, very different from the CO₂-rich geochemical environment of the BAS area. It is therefore likely that a quenching effect could explain the shift towards more positive $\delta^{13}C$ values of methane in the BAS data that "freezes" the isotopic equilibrium at corresponding higher temperatures. Assuming that a quenching effect is significant on the BAS samples, the consequences are equally important; under this hypothesis the temperature would have a corresponding isotopic equilibrium in the range estimated by the equation (8), that is between 370 and 515°C and, in turn, such high temperatures can be explained by deep magmatic inputs.

5.5 Temporal variations of $^3He/^4He$ in gases from Mayotte

In order to have further evidences of possible variations of geochemical parameters that may have recorded the ongoing submarine volcanic activity, we evaluated the time variation of the helium isotope ratio. This tracer was found to be crucial in defining magmatic recharge in deep reservoirs in many volcanic systems on Earth (Boudoire et al., 2020; Caracausi et al., 2003; Sano et al., 2015; Paonita et al., 2016; Rizzo et al., 2015, 2016). Figure 6 shows values from the 2008 (BRGM repository) and the 2018-2019 surveys. As discussed before, the interpretation of this parameter is quite complex in the Comoros context, because of the possible "low- $^3He/^4He$ " signature of the deeper undegassed astenospheric source. Our data suggests that the helium isotopic signature of the BAS fluids (Figure 8) was relatively low in the 2008 samples and it becomes significantly higher (average increase of 0.58 Rc/Ra) in the samples from the 2018 survey. This shift is consistent with the drainage of large volumes of evolved basanite magma from shallow mantle lithospheric depth feeding the Mayotte gaseous emissions at least in 2008, whose potential signature is very close to that recorded by fluid inclusions at La Grille (Class et al., 2005). Since the beginning of the eruption, the Rc/Ra signature of BAS fluids approaches that conventionally accepted for convective MORB mantle (8 ± 1 Ra, Graham, 2002). Thus, we can tentatively speculate that this time evolution is associated with the emplacement of sub-lithospheric magmas at shallower depth along the large Mayotte volcanic ridge.



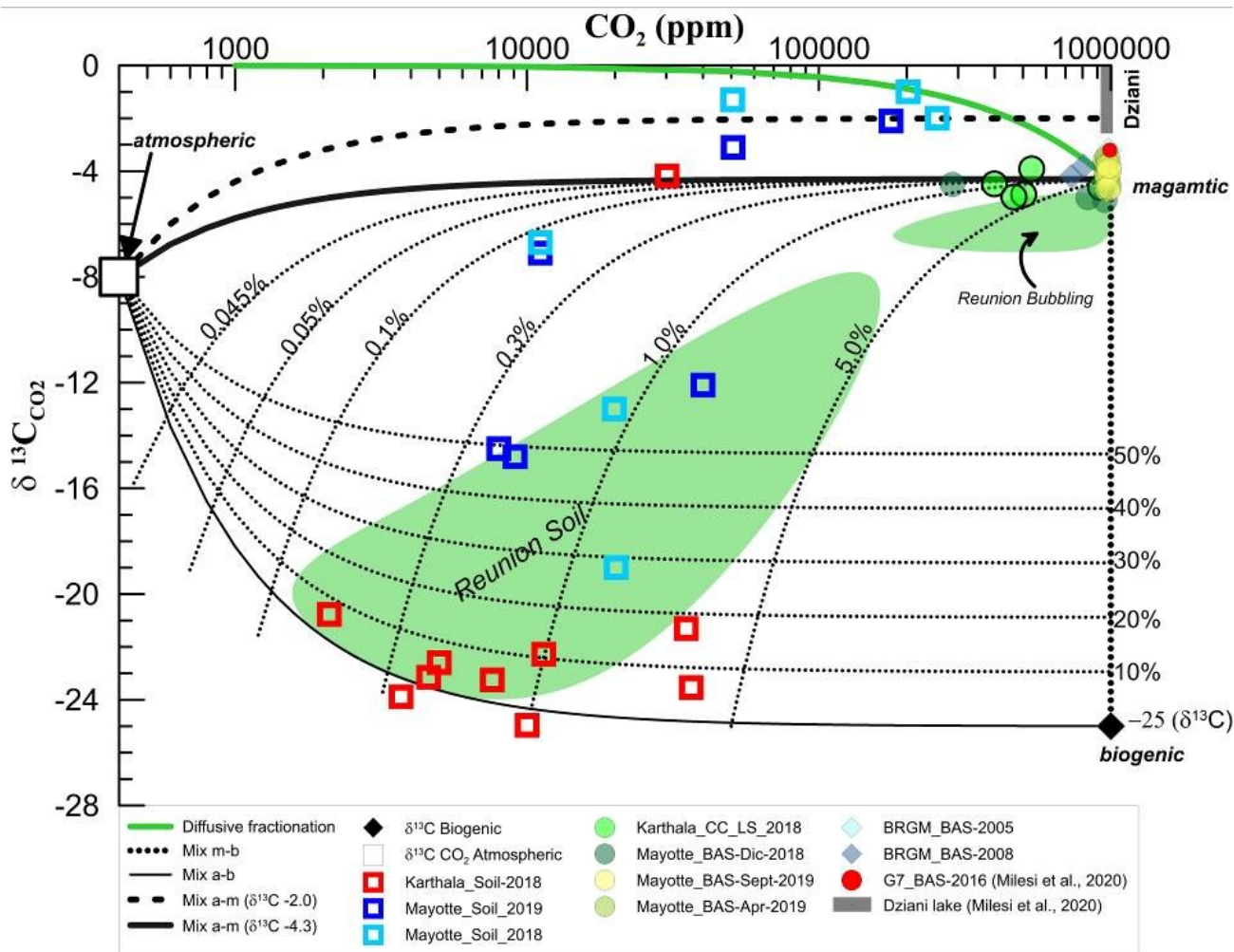
779 Figure 8. Rc/Ra time series with symbols as in figure 3. Rc/Ra has increased by an average 0.5 of between 2008 and
780 2018-2019. Black dashed lines indicate the averages Rc/Ra for the two distinct periods.

781

782 **5.6 Gas emissions from the soil**

783 Soil CO₂ emission can be ascribed to various origins and generally the total outgassing budget
784 results from a mixture of different sources (Amundson et al., 1998; Cerling et al., 1991; Chiodini et
785 al., 2008; Liuzzo et al. 2015). With the aim at quantifying the different contributions other than
786 those of magmatic origin, such as biogenic source or air contamination in soil CO₂ flux, 22 gas
787 samples were collected at Grande Comore and at Mayotte for CO₂ concentration and carbon
788 isotopic analysis ($\delta^{13}\text{C}_{\text{CO}_2}$) (table 1). All the samples were taken directly at 0.5 m depth in the soil, as
789 described in section 3.2. The results of their CO₂ concentration and C isotopic signature are shown
790 in Figure 9, and are modelled as a mixing of three possible endmembers: atmospheric, biogenic
791 and magmatic. Figure 9 also reports $\delta^{13}\text{C}$ of gas from fumarolic fields at Karthala (central crater CC
792 and La Soufrière LS, Figure 5B) and from the bubbling marine area off the coast at Mayotte (BAS,
793 Figure 6), both obtained from the 2017-2018 surveys. Included in Figure 9 are also data collected
794 at Mayotte by BRGM in 2005-2008 (BRGM/RP-568082 Final reports 2008) and in 2016 from Milesi
795 et al. (2020) at the Dziani volcanic lake, with the exception of sample G7 that was collected in 2016

796 at the bubbling area BAS. We report the endmembers of atmospheric ($\delta^{13}\text{C} = -8\text{‰}$) and “biogenic”
797 ($\delta^{13}\text{C} = -25\text{‰}$; Hoefs, 2015) carbon (corresponding to organic matter). In Figure 9, we report the
798 mixing curves between the three endmembers reported above. The effect of dissolution in water
799 on the CO₂ emission from the soil, if any, is not included here, and in every cases it should be
800 modest. The “magmatic” endmember was fixed considering the $\delta^{13}\text{C}$ average values of CO₂ of
801 fumarolic and bubbling gases from Karthala and Mayotte, which we considered representative of
802 the magmatic signature beneath these islands of the Comore Archipelago ($\delta^{13}\text{C} = -4.3\text{‰}$). This
803 choice is supported by the small narrow variability of $\delta^{13}\text{C}$ range of variation both in at Karthala
804 fumaroles ($-4.9\text{‰} \leq \delta^{13}\text{C} \leq -3.9\text{‰}$) and Mayotte BAS high flux bubbling pools least affected by gas-
805 water interaction ($-4.9\text{‰} \leq \delta^{13}\text{C} \leq -3.5\text{‰}$, slightly higher values up to 5.7 being those of the MAN low
806 flux pool), and their relatively stability in time considering data from BRGM of 2006 and 2008
807 campaigns ($-4.3\text{‰} \leq \delta^{13}\text{C} \leq -3.2\text{‰}$) as well as in 2016 with $\delta^{13}\text{C} = -3.2\text{‰}$ (G7 point by Milesi et al.,
808 2020), thus a reasonable approximation of a possible $\delta^{13}\text{C}$ magmatic signature for the Archipelago.
809 The effect of dissolution in water of the CO₂ emission from the soil it is not considered here
810 because could be considered modest.



811

812 Figure 9. Diagram plotting carbon isotopic composition of soil CO₂ versus soil CO₂ log-concentrations (ppm) showing
 813 the theoretical binary mixing curves between three endmembers: atmospheric, biogenic and magmatic. Also shown
 814 are the binary mixing curves (hyphen curve) which allow a differentiation in the percentage of the magmatic
 815 component (M) in the hypothesis that the biogenic contribution could be extended up to δ¹³C 25‰ (Hoefs, 2015).
 816 Green areas are referred to La Reunion soil and bubbling gases data repository, while the grey bar is the δ¹³C_(CO₂)
 817 Diziani lake's variability from Milesi et al., (2020).

818 The Karthala isotopic signature regarding δ¹³C in CO₂ from the soil is much wider than in the
 819 fumaroles and ranges in the interval -24.9‰ ≤ δ¹³C ≤ -4.2‰. Almost all of the isotopic values show a
 820 low contribution of magmatic gas and a variable degree of air contamination. A few samples
 821 showing high CO₂ concentration have however a modest magmatic contribution (less than 20%)
 822 and correspond to sites close to the main structural lineaments showed in Figure 7. A single δ¹³C
 823 value from the soil at Karthala has an isotopic signature close to the magmatic endmember and
 824 the corresponding site is very close to the steaming fumarolic field inside the summit CC caldera.
 825 These results allow us to conclude that during the 2017 and 2018 surveys, which were performed
 826 during a phase of quiescence of the volcano, soil CO₂ emission on the flanks at Grande Comore was
 827 predominantly of biogenic origin, while clear evidence of volcanic origin CO₂ emission was
 828 detectable only at the summit crater of Karthala. This overall picture of gas fluxes and isotopic

signature at Karthala is in strong contrast with that found during a similar quiescence period at Piton de la Fournaise (Liuzzo et al., 2015). On Piton de la Fournaise, only weak emission of low-temperature fluids and low CO₂ fluxes occur in the central summit area during quiescence periods, while diffuse CO₂ emissions with a clear and strong magmatic contribution (up to 60% of the diffuse fluid composition) have been detected along the main rift zones on the flanks of the volcano. On both volcanoes deep fluid percolation is focused on the main rift zones crossing the volcano edifice. However, the much lower rate of volcanic activity and longer quiescence duration at Karthala translates in low soil CO₂ fluxes with a dominant organic signature. The absence of permanent CO₂-rich emissions below the summit area of Piton de la Fournaise has been attributed to the geometry of its deep plumbing system, which is laterally shifted with respect to the central summit area (Liuzzo et al., 2015; Michon et al., 2015).

At Mayotte the isotopic values of soil gases taken on land are much more scattered than the Karthala data sampled on the volcano flanks. The range of isotopic variation spans the 19.0‰ ≤ δ¹³C ≤ -1‰ range at various CO₂ concentrations. In contrast with Karthala soil emissions, those from Mayotte show a significant magmatic contribution. It is interesting to notice a scattered distribution similar to that previously reported for δ¹³C in soil emission at La Reunion (Boudoire et al, 2017; Liuzzo et al, 2015). The Comoros archipelago is located in the Equatorial rainforest climate zone and La Réunion in a rainy tropical context. Therefore it is reasonable to consider that the soil of these islands is characterised by similar paedogenesis and biogenic processes to those identified in other tropical zones (Basile-Doelsch et al., 2005; Frank et al., 2002, 2006; Rouff et al., 2012), which in turn can significantly affect the isotopic signature of carbon in soil CO₂, as reported at La Reunion by Liuzzo et al. (2015). It is therefore not surprising that δ¹³C of CO₂ distribution in Mayotte lies within a comparable range of values as those reported for isotopic soil CO₂ measurements at La Reunion in previous works (Boudoire et al 2017, Liuzzo et al. 2015). Interestingly, in terms of soil emissions, the fluid composition and fluxes of Mayotte, where a huge submarine eruption is occurring, mimic those measured on the other very active volcano of the Indian ocean, Piton de la Fournaise.

The less negative δ¹³C values (-3‰ < δ¹³C < -1‰) were recorded at several soil CO₂ sampling areas that were taken on the beach or on a cliff very close to the BAS bubbling zone. However, these values cannot be explained as a mixing of atmospheric and magmatic CO₂ fixed at -4.3‰. The less negative δ¹³C values for these two sites elicit three possible hypotheses: either 1) they may lie in a

860 mixing curve between atmospheric and magmatic endmember where the magmatic signature is
 861 more positive (around $\delta^{13}\text{C} = -2\text{‰}$); 2) they can be affected by isotopic fractionation on the aquifer;
 862 or 3) they are affected by kinetic fractionation due to a process of CO_2 diffusion through the soil as
 863 observed in other studies (Capasso et al., 2001; Cerling, 1984; Hesterberg and Siegenthaler, 1991;
 864 Severinghaus et al., 1996). We stress that we identify this process only in a limited area, very close
 865 to the BAS tidal flat, which is affected by a process determining a significant modification of the
 866 isotopic signature that ends with less negative $\delta^{13}\text{C}$ value. Regarding the first hypothesis, a mixing
 867 curve between air and magmatic endmember fixed at $\delta^{13}\text{C} = -2\text{‰}$ seems to correlate well to these
 868 more positive isotopic data (black dashed curve in Figure 9). In addition, the mixing curve at $\delta^{13}\text{C} = -$
 869 2‰ lies in the range of isotopic signatures of Dziani lake (Milesi et al., 2020). However, Dziani lake
 870 lies within a closed volcanic crater that receives a significant volcanic CO_2 contribution. According
 871 to Milesi et al. (2019) also in such lacustrine site biogenic and microbial methanogenesis CO_2
 872 reduction is particularly significant (thus potentially affecting the isotopic signature of CO_2 shifting
 873 $\delta^{13}\text{C}$ toward more positive signature. These microbial processes have not been identified in our
 874 beach context. The similarity of the $\delta^{13}\text{C}$ signature between Dziani lake and these few ground sites
 875 discussed is unrealistic also because the mentioned soil degassing area is far from Dziani lake,
 876 while instead very close to the BAS (a few tens of meters). As a consequence, we should expect an
 877 isotopic signature closer to that measured in BAS fluids. Moreover, it is difficult to explain
 878 alongside the entire dataset presented here, especially considering that the Karthala data fall
 879 within a range comparable to the bubbling data at Petite Terre. The second hypothesis invokes an
 880 isotopic fractionation that may be ascribed to the interference with the (salty) aquifer, which in
 881 turn should determine more negative isotopic values. In addition, the composition of soil gas
 882 samples collected at Mayotte do not show detectable CO_2 dissolution in water (see Figure S1
 883 supplementary), therefore the interference of the aquifer at this site seems to be very modest.
 884 Regarding the third hypothesis, a curve of diffusive fractionation was modelled (green line in
 885 Figure 9) following Capasso et al. (2001):

$$\delta_i = -\Delta_x \cdot \left(\frac{D_{j-a}}{D_{i-a}} - 1 \right) \cdot 10^3 \text{‰} \quad (9)$$

887 where δ_i is the expected fractionated isotopic value of soil CO_2 sample; Δ_x is the variable molar
 888 fraction between CO_2 in air and in the sample; D is the binary diffusion coefficient of CO_2 in air;
 889 where specifically, D_j is related to ^{12}C , and D_i is related to ^{13}C . In our case, the diffusivity ratio of

890 carbon in CO₂ (by the way D_{j-a}/D_{i-a}) is equal to 1.0044 (from Reid et al., 1977). For these samples,
891 which were collected in the area close to the bubbling zone, it is therefore reasonable to consider
892 a variable grade of isotopic diffusive fractionation that modified gases with a starting isotopic
893 signature probably close to the bubbling gas thus leading to the conclusion that a kinetic diffusive
894 fractionation might be the main process acting in this specific zone of the island.

895 We are aware that a wider dataset would certainly contribute to a more comprehensive
896 understanding of the various processes responsible of the isotopic signature in soil CO₂ gas at
897 Petite Terre. We however underline that the most significant results from this dataset support the
898 hypothesis of a clear fingerprint of an active magmatic source into soil CO₂ emissions which has
899 not been clearly identified on the volcano flanks of Karthala. Consequently, we conclude that the
900 high CO₂ fluxes from the BAS tidal area and the time evolution of their He isotopic signature,
901 together with the stronger magmatic CO₂ contribution emissions diffused on land at Petite Terre,
902 potentially record the large magmatic and volcanic event occurring on the submarine flanks of the
903 island. On the contrary, we can anticipate that the future reactivation of Karthala volcano should
904 be recorded by a significant change in CO₂ emissions from the soil in terms of both fluxes, areal
905 distribution and isotopic composition, as observed on other active volcanoes (Liuzzo et al. 2013).

906 6. Conclusion

907

908 This work presents the results of recent campaigns for the measurement of soil, fumarolic and
909 bubbling gas emissions in two islands within the Comoros archipelago: Grande Comore and
910 Mayotte. Although the measurement campaigns of soil CO₂ emissions are not exhaustive for the
911 entire territory of these two islands, the first results show that they are spatially distributed along
912 the main structural features of both Grande Comore and Petite Terre. A significant difference is
913 found in the origin of the CO₂ emitted from the soil. The carbon isotopic signature of soil CO₂
914 emissions highlights evidence of a low magmatic contribution at distal areas of Karthala volcano,
915 and a significantly higher magmatic contribution in CO₂ emissions at Petite Terre.

916 Gas geochemistry of fumarolic fields at Karthala (Grande Comore), and bubbling gases at Mayotte
917 fall within the typical range of MORB-type mantle source. Compared with La Reunion dataset
918 (Liuzzo et al., 2015; Boudoire et al., 2018), the Comoros islands dataset shows a CH₄ enrichment,
919 and a variable degree of air contamination.

920 The isotopic signature of helium ($^3\text{He}/^4\text{He}$) in gas emissions confirms relatively low Rc/Ra values
921 (4.18-7.53) for the entire archipelago compared to other volcanic systems in the Indian Ocean
922 such as Reunion (12-14.6). $^3\text{He}/^4\text{He}$ data are consistent with average values of fluid inclusions for
923 both Karthala and Petite Terre, spanning in the interval of $6.41 \leq \text{Rc/Ra} \leq 7.53$ at Petite Terre and
924 $4.68 \leq \text{Rc/Ra} \leq 5.87$ at Karthala. The origin of CO_2 in the fumarolic emissions is basically magmatic
925 (-5.7; -3.2) with no evidence of significant organic or sedimentary contribution for both Grande
926 Comore and Mayotte.

927 Based on the CO_2 , H_2 , H_2O and CH_4 contents, a hydrothermal system below Mayotte has been
928 recognized with an equilibrium temperature of $\sim 300^\circ\text{C}$. Water-gas interaction process has been
929 detected in Mayotte resulting in a partial CO_2 dissolution in water. The methane of the
930 hydrothermal system seems to be abiogenic in origin.

931 The differences recognized between Grande Comore and Mayotte may be ascribed to the different
932 states of volcanic activity at the two islands at the time of the surveys. Soil CO_2 emissions at
933 Grande Comore are generally dominated by biogenic origin while there is a clear magmatic CO_2
934 contribution in Petite Terre.

935 Moreover, the increased value of Rc/Ra between 2008 and 2018-19 at Mayotte coupled to a not
936 fully-reached isotopic equilibrium of the pair $\delta^{13}\text{C}_{\text{CO}_2}$ - $\delta^{13}\text{C}_{\text{CH}_4}$ in the hydrothermal fluids may be
937 ascribed to the recent volcanic activity which generated the new submarine volcano 45 km
938 offshore from Petite Terre.

939 Further investigations and a suitable geochemical monitoring program are needed to better
940 understand the complex volcanic system of Comoros archipelago. Nevertheless, our results show
941 some clues of a potential volcano activity of Mayotte which opens important scenarios for the
942 implication regarding procedures aimed to reduce volcanic hazard in this region.

943 Acknowledgments

944 This work is part of the PhD (XXXIV cycle) of Marco Liuzzo at the University of Ferrara. The work
945 has been partially founded by INGV (GECO project Fondi Ricerca libera 2019 INGV) and by
946 REVOSIMA Initiative (IPGP, CNRS, BRGM, IFREMER) for fieldwork and analytical activities. We are
947 grateful to CNDRS of Moroni for the local assistance to our team, as well as thankful to the
948 Interreg Hatari support to A. Di Muro e B. Shafik. All datasets for this research are included in this
949 paper (and its supplementary information files) and listed in tables 1-3 and table S1. Dataset not

950 included in the mentioned tables, which are showed in the figures 3, 4, 7, 9, S2, are available
951 through the inside references cited and also listed in the final reference section.
952 The authors are very thankful to P. Allard for lending us the accumulation chamber for soil CO₂
953 surveys and C. Ventura Bordenga for his invaluable support on the Karthala field. We also thank
954 INGV, Sezione di Palermo, for allowing the access to the analytical facilities. In particular, we are
955 grateful to S. Cappuzzo who provided some of the technical equipment, F. Salerno and M. Longo
956 for performing analyses of gases chemistry, M. Tantillo and M. Misseri for carrying out the noble
957 gases isotopic measurements in the laboratory, G. Capasso, Y. Oliveri and A. Sollami for providing
958 CO₂ and CH₄ isotopic analysis in the stable isotopes laboratory.

959

960 [References](#)

- 961 Amundson, R., Stern, L., Baisden, and Wang, Y. (1998) The isotopic composition of soil and soil-
962 respired CO₂, *Geoderma*, 82, 83–114
- 963 Bachelery, P., Berthod, C., Di Muro, A., Gurioli, L., Besson, P., Caron, B., ... & Jorry, S. (2019,
964 December). Petrological and Geochemical Characterization of the Lava from the 2018-2019
965 Mayotte Eruption: First Results. *AGU Fall Meeting Abstracts* (Vol. 2019, pp. V52D-06).
- 966 Bachèlery, P., and Hémond, C. (2016) Geochemical and Petrological Aspects of Karthala Volcano
967 In: Bachèlery, P., Lénat, J.-F., Di Muro, A., Michon, L. (Eds.), *Active Volcanoes of the Southwest*
968 *Indian Ocean: Piton de La Fournaise and Karthala*. Springer-Verlag, Berlin and Heidelberg, pp. 367–
969 384
- 970 Bachèlery, P., Coudray, J. (1993) Carte volcano-tectonique (1/50000e) de la Grande Comore et
971 notice explicative. Edited by the French Embassy in Moroni, Comoros, and The University of La
972 Réunion, St. Denis de La Réunion
- 973 Bachèlery, P., Morin, J., Villeneuve, N., Soulé, H., Nassor, H. and Radadi Ali, A. (2016) Structure and
974 Eruptive History of Karthala Volcano. In: Bachèlery, P., Lénat, J.-F., Di Muro, A., Michon, L. (Eds.),
975 *Active Volcanoes of the Southwest Indian Ocean: Piton de La Fournaise and Karthala*. Springer-
976 Verlag, Berlin and Heidelberg, pp. 345–366
- 977 Baker, J. F. and Fritz, P. (1981) Carbon isotope fractionation during microbial methane oxidation.
978 *Nature* 293, 289-291
- 979 Basile-Doelsch, I., Amundson, R., Stone, W. E. E., Masiello, C. A., Bottero, J. Y., Colin, F., et al.
980 (2005), Mineralogical control of organic carbon dynamics in a volcanic ash soil on La Reunion, *Eur.*
981 *J. Soil Sci.*, 56, 689–703, doi:10.1111/j.1365-2389.2005.00703.x

982 Bassias, Y., & Leclaire, L. (1990) The Davie Ridge in the Mozambique Channel: crystalline basement
983 and intraplate magmatism, *Neues Jahrbuch für Geologie und Paläontologie*, 4, 67–90

984 Batista Cruz, R. Y., Rizzo, A. L., Grassa, F., Bernard Romero, R., González Fernández, A.,
985 Kretzschmar, T. G., & Gómez–Arias, E. (2019). Mantle degassing through continental crust
986 triggered by active faults: The case of the Baja California Peninsula, Mexico. *Geochemistry,*
987 *Geophysics, Geosystems*, 20. <https://doi.org/10.1029/2018GC007987>

988 Benavente, O., and Brotheridge, J. (2015) Comoros surface exploration. Geochemistry, soil CO₂
989 flux and shallow temperature surveys. New Zealand Ministry of Foreign Affairs and Trade (MFAT).
990 Jacobs. 65pg.

991 Bernabeu, N., Finizola, A., Smutek, C., Saramito, P., & Delcher, E. (2018). Spatio-temporal evolution
992 of temperature and fluid flow through a new “thermo-lithological” boundary; the case of a pit
993 crater of Karthala volcano (Comoros archipelago) refilled on January 13th 2007 by a lava flow.
994 *Journal of Volcanology and Geothermal Research*, 367, 7-19.
995 <https://doi.org/10.1016/j.jvolgeores.2018.10.013>

996 Berthod, C., Médard, E., Bachèlery, P., Gurioli, L., Di Muro, A., Peltier, A., ... & Feuillet, N. (2020,
997 December). The 2018-ongoing Mayotte submarine eruption: magma migration imaged by
998 petrological monitoring. *AGU Fall Meeting*, 1-17 décembre 2020.

999 Bonforte, A., Federico, C., Giammanco, S., Guglielmino, F., Liuzzo, M., Neri, M., 2013. Soil gases
1000 and SAR measurements reveal hidden faults on the sliding flank of Mt. Etna (Italy). *J. Volcanol.*
1001 *Geotherm. Res.* 251, 27–40

1002 Bottinga, Y. (1969) Calculated fractionation factors for carbon and hydrogen isotope exchange in
1003 the system calcite-carbon dioxide-graphite-methane hydrogen-water vapor. *Geochim. Cosmochim.*
1004 *Acta* 33, 49-64

1005 Boudoire, G., Finizola, A., Di Muro, A., Peltier, A., Liuzzo, M., Grassa, F., et al. (2018a) Small-scale
1006 spatial variability of soil CO₂ flux: Implication for monitoring strategy. *Journal of Volcanology and*
1007 *Geothermal Research*. Volume 366. ISSN 0377-0273.
1008 <https://doi.org/10.1016/j.jvolgeores.2018.10.001>

1009 Boudoire, G., Liuzzo, M., Di Muro, A., Ferrazzini, V., Michon, L., Grassa, F., Derrien, A., et al. (2017)
1010 Investigating the deepest part of a volcano plumbing system: evidence for an active magma path
1011 below the western flank of Piton de la Fournaise (La Reunion Island). *J. Volcanol. Geotherm. Res.*
1012 <https://doi.org/10.1016/j.jvolgeores.2017.05.026>

1013 Boudoire G., Rizzo, A. L., Di Muro, A., Grassa, F. & Liuzzo, M. (2018b) Extensive CO₂ degassing in
1014 the upper mantle beneath oceanic basaltic volcanoes: First insights from Piton de la Fournaise
1015 volcano (La Réunion Island). *Geochimica et Cosmochimica Acta* 235, 376–401

1016 Boudoire G., Rizzo, A.L., Arienzo, I. et al. (2020) Paroxysmal eruptions tracked by variations of
1017 helium isotopes: inferences from Piton de la Fournaise (La Réunion island). *Sci Rep* 10, 9809
1018 (2020). <https://doi.org/10.1038/s41598-020-66260-x>

1019 BRGM/RP-568082 Final reports 2008 – Sanjuan, B., Baltassat, J. F. – Estimation du potentiel
 1020 géothermique de Mayotte: Phase 2 – Etape 2. Investigations.-M., Bezelgues S., Brach M., Girard J.-
 1021 F., Mathieu géologiques, géochimiques et géophysiques complémentaires, synthèse des résultats

1022 Camarda, M., Gurrieri, S., and Valenza, M. (2006a) CO₂ flux measurements in volcanic areas using
 1023 the dynamic concentration method: Influence of soil permeability, *J. Geophys. Res.*, 111, B05202,
 1024 Doi:10.1029/2005JB003898

1025 Camarda, M., Gurrieri, s., and Valenza, M. (2006b), In situ permeability measurements based on a
 1026 radial gas advection model: Relationships between soil permeability and diffuse CO₂ degassing in
 1027 volcanic areas, *Pure Appl. Geophys.*, 163(4), 897–914, doi:10.1007/s00024-006-0045-y

1028 Capasso, G., D'Alessandro, W., Favara, R., Inguaggiato, S., Parello, F. (2001) Kinetic isotope
 1029 fractionation of CO₂ carbon due to diffusion processes through the soil. *Water-Rock Interaction*
 1030 10. Swets & Zeitlinger, Lisse

1031 Caracausi A., Italiano, F., Paonita, A., Rizzo, A., and Nuccio, P. M. (2003), Evidence of deep magma
 1032 degassing and ascent by geochemistry of peripheral gas emissions at Mount Etna (Italy):
 1033 Assessment of the magmatic reservoir pressure, *J. Geophys. Res.*, 108(B10), 2463,
 1034 doi:10.1029/2002JB002095

1035 Cerling, T.E. (1984) The stable isotopic composition of modern soil carbonate and its relationship
 1036 to climate Earth. *Planet. Sci. Lett.*, 71 (1984), pp. 229-240

1037 Cerling, T. E., Solomon, D. K., Quade, J., and Bowman, J. R. (1991) On the isotopic composition of
 1038 carbon in soil carbon dioxide, *Geochim. Cosmochim. Acta*, 55, 3403–3405

1039 Cesca, S., Letort, J., Razafindrakoto, H. N., Heimann, S., Rivalta, E., Isken, M. P., Nikkhoo, M.,
 1040 Passarelli, L., Petersen, G. M., Cotton, F., & Dahm, T., 2020. Drainage of a deep magma reservoir
 1041 near Mayotte inferred from seismicity and deformation. *Nature Geoscience*, 13(1), 87-93

1042 Chaheire, M., Chamassi, M., and Houmadi, N. (2016) GEOTHERMAL DEVELOPMENT IN THE
 1043 COMOROS AND RESULTS OF GEOTHERMAL SURFACE EXPLORATION - Proceedings, *6th African Rift*
 1044 *Geothermal Conference* Addis Ababa, Ethiopia, 2nd – 4th November 2016

1045 Chiodini, G., Cioni, R., Guidi, M., Marini, L. & Raco, B. (1998) - Soil CO₂ flux measurements in
 1046 volcanic and geothermal areas. *Appl. Geochem.*, 13, 534–552

1047 Chiodini, G. and Marini, L. (1998), Hydrothermal gas equilibria: The H₂O-H₂-CO₂-CO-CH₄ system,
 1048 *Geochim. Cosmochim. Acta*. 62, 2673–2687

1049 Chiodini, G., Caliro, S., Cardellini, C., Avino, R., Granieri, D., and Schmidt, A. (2008), Carbon isotopic
 1050 composition of soil CO₂ efflux, a powerful method to discriminate different sources feeding soil
 1051 CO₂ degassing in volcanic-hydrothermal areas, *Earth Planet. Sci. Lett.*, 274(3–4), 372–379,
 1052 doi:10.1016/j.epsl.2008.07.051

- 1053 Clark, I. D., and Fritz, P. (1997). *Environmental Isotopes in Hydrogeology*. Boca Raton, FL: CRC
1054 Press, 328
- 1055 Class, C, Goldstein, S.L. (1997) Plume-lithosphere interactions in the ocean basins: constraints from
1056 the source mineralogy. *Earth Planet Sci Lett* 150:245–260
- 1057 Class, C, Goldstein, S.L., Altherr, R., Bachelery, P. (1998) The process of plume—lithosphere
1058 interactions in the Ocean Basins—the case of Grande Comore. *J Petrol* 39(5):881–903
- 1059 Class, C., Goldstein, S.L., Shirey, S.B. (2009) Osmium in Grande Comore lavas: a new extreme among
1060 a spectrum of EM-type mantle endmembers. *Earth Planet Sci Lett* 284:219–227
- 1061 Class, C., Goldstein, S.L., Stute, M., Kurz, M.D., Schlosser, P. (2005) Grand Comore Island: a well-
1062 constrained “low 3He/4He”. *Earth Planet Sci Lett* 233:391–409
- 1063 Claude-Ivanaj, C., Bourdon, B., Allègre, C.J. (1998) Ra-Th-Sr isotope systematic in Grande Comore
1064 Island: a case study of plume-lithosphere interaction. *Earth Planet Sci Lett* 164:99–117
- 1065 Coffin, M. F., Rabinowitz, P. D., & Houtz, R. E., (1986). Crustal structure in the western Somali
1066 Basin. *Geophysical Journal International*, 86(2), 331–369
- 1067 Coleman, D. D., Risatti, J. B. and Schoell, M. (1981) Fractionation of carbon and hydrocarbon
1068 isotopes by methane-oxidizing bacteria. *Geochim. Cosmochim. Acta* 45, 1033–1037
- 1069 Coltorti, M., Bonadiman, C., Hinton, R.W., Siena, F., Upton, B.G.J. (1999) Carbonatite
1070 metasomatism of the oceanic upper mantle: evidence from clinopyroxenes and glasses in
1071 ultramafic xenoliths of Grande Comore, Indian Ocean. *J. Petrol* 40:133–165
- 1072 Courtillot, V., Davaille, A., Besse, J., Stock, J. (2003) Three distinct types of hotspots in the Earth’s
1073 mantle. *Earth Planet Sci Lett* 205:295–308
- 1074 D’Amore, F., and Panichi, C. (1980). Evaluation of deep temperature of hydrothermal systems by a
1075 new gas geothermometer. *Geochim. Cosmochim. Acta* 44, 549–556. doi: 10.1016/0016-
1076 7037(80)90051-4
- 1077 Debeuf, D. (2004) Etude de l’évolution volcano-structurale et magmatique de Mayotte (Archipel
1078 des Comoros, Océan Indien): Approches structurale, pétrographique, géochimique et
1079 géochronologique. Unpublished Ph.D. thesis, Université de La Réunion, 243 pp
- 1080 Deniel, C. (1998) Geochemical and isotopic (Sr, Nd, Pb) evidence for plume-lithosphere
1081 interactions in the genesis of Grande Comore magmas (Indian Ocean). *Geochem Geol* 144:281–303
- 1082 Emerick, C.M., & Duncan, R.A. (1982) Age progressive volcanism in the Comoros Archipelago,
1083 eastern Indian Ocean and implications for Somali plate tectonics, *Earth Planet Sci Lett* 60(3), 415–
1084 428
- 1085 Evans, W.C, Sorey, M.L., Kennedy, B.M., Stonestrom, D.A., Rogie, J.D., Shuster, D.L. (2001) High
1086 CO₂ emissions through porous media: transport mechanisms and implications for flux

1087 measurement and fractionation. *Chemical Geology*, Volume 177, Issues 1–2, 2001, Pages 15-29,
 1088 ISSN 0009-2541, [https://doi.org/10.1016/S0009-2541\(00\)00379-X](https://doi.org/10.1016/S0009-2541(00)00379-X)

1089 Famin, V., Michon, L., & Bourhane, A., 2020. The Comoros archipelago: a right-lateral transform
 1090 boundary between the Somalia and Lwandle plates. *Tectonophysics*,
 1091 doi.org/10.1016/j.tecto.2020.228539

1092 Feuillet, N. et al., 2019. Birth of a large volcano offshore Mayotte through lithosphere-scale
 1093 rifting, in *Proceedings of the AGU Fall Meeting 2019*. AGU

1094 Fischer, T. P. and Chiodini, G., 2015. Volcanic, magmatic and hydrothermal gases. In *The*
 1095 *Encyclopedia of Volcanoes*, 2nd edn. *Academic Press, Elsevier, Waltham*, pp. 779–796,
 1096 [doi:10.1016/B978-0-12-385938-9.00045-6](https://doi.org/10.1016/B978-0-12-385938-9.00045-6)

1097 Frank, A. B., Liebig, M. A., and Hanson, J. D. (2002), Soil carbon dioxide fluxes in northern semiarid
 1098 grasslands, *Soil Biol. Biochem.*, 34, 1235–1241. Frank, A. B., M. A. Liebig, and D. L. Tanaka (2006),
 1099 Management effects on soil CO₂ efflux in northern semiarid grassland and cropland, *Soil Tillage*
 1100 *Res.*, 89, 78–85, [doi:10.1016/j.still.2005.06.009](https://doi.org/10.1016/j.still.2005.06.009)

1101 French, S. W., & Romanowicz, B. (2015). Broad plumes rooted at the base of the Earth's mantle
 1102 beneath major hotspots. *Nature*, 525(7567), 95–99.

1103 Gaina, C., Torsvik, T. H., van Hinsbergen, D. J. J., Medvedev, S., Werner, S. C., and Labails, C. (2013),
 1104 The African Plate: A history of oceanic crust accretion and subduction since the Jurassic,
 1105 *Tectonophysics*, 604, 4–25

1106 Gérard, E., De Goeyse, S., Hugoni, M., Agogué, H., Richard, L., Milesi, V., et al. (2018). Key role of
 1107 alphaproteobacteria and cyanobacteria in the formation of stromatolites of Lake Dziani Dzaha
 1108 (Mayotte, Western Indian Ocean). *Frontiers in microbiology*, 9, 796.

1109 Giammanco, S., Gurrieri, S., and Valenza, M. (2006), Fault controlled soil CO₂ degassing and
 1110 shallow magma bodies: Summit and lower East Rift of Kilauea Volcano (Hawaii), 1997, *Pure Appl.*
 1111 *Geophys.*, 163(4), 853–867, [doi:10.1007/s00024-006-0039-9](https://doi.org/10.1007/s00024-006-0039-9)

1112 Giggenbach, W. F. (1982) Carbon-13 exchange between CO₂ and CH₄ under geothermal
 1113 conditions. *Geochim. Cosmochim. Acta* 46, 159–165

1114 Giggenbach, W. F. (1992) Chemical techniques in geothermal exploration. Applications of
 1115 geochemistry in geothermal reservoir development (F. D'Amore ed.) UNITAR/UNDP Centre on
 1116 *Small Energy Resources*. pp. 119–143, Rome

1117 Giggenbach, W.F., and Goguel, R.L., 1989, Methods for the collection and analysis of geothermal
 1118 and volcanic water and gas samples: New Zealand Department of Scientific and Industrial
 1119 Research, Chemistry Division Report 2387, 53 p

1120 Gurrieri, S., & Valenza, M. (1988) - Gas transport in natural porous mediums: A method for
 1121 measuring CO₂ flows from the ground in volcanic and geothermal areas. *Rend. Soc. Ital. Mineral.*
 1122 *Petrol.*, 43, 1151–1158

- 1123 Gurrieri, S., Liuzzo, M., and Giudice, G. (2008), Continuous monitoring of soil CO₂ flux on Mt. Etna:
1124 The 2004–2005 eruption and the role of regional tectonics and volcano tectonics, *J. Geophys. Res.*,
1125 113, B09206, doi:10.1029/2007JB005003, 2008
- 1126 Hajash, A., Armstrong, R.L. (1972) Paleomagnetic and radiometric evidence for the age of the
1127 Comoros Islands, West Central Indian Ocean. *Earth Planet Sci Lett* 16:231–236
- 1128 Hesterberg, and Siegenthaler (1991) Production and stable isotopic composition of CO₂ in a soil
1129 near Bern, Switzerland *Tellus*, 43B (1991), pp. 197-205
- 1130 Hoefs, J. (2015) Stable Isotope Geochemistry. Seventh Edition, 208 pp., *Springer International*
1131 *Publishing Switzerland* 2015. ISBN 978-3-319-19715-9. DOI 10.1007/978-3-319-19716-6
- 1132 Horita, J. (2001) Carbon isotope exchange in the system CO₂-CH₄ at elevated temperatures.
1133 *Geochimica et Cosmochimica Acta*, Vol. 65, No. 12, pp. 1907–1919, 2001
- 1134 Hugoni, M., Escalas, A., Bernard, C., Nicolas, S., Jezequel, D., Vazzoler, F., et al. (2018).
1135 Spatiotemporal variations in microbial diversity across the three domains of life in a tropical
1136 thalassohaline lake (Dziani Dzaha, Mayotte Island). *Molecular ecology*, 27(23), 4775-4786.
- 1137 Hulston, J. R., and McCabe, W. J. (1962) Mass spectrometer measurements in the thermal areas of
1138 New Zealand. Part 2. Carbon isotopic ratios. *Geochim. Cosmochim. Acta* 26, 399-410
- 1139 Irwin, W. P., and Barnes, I. (1980), Tectonic relations of carbon dioxide discharges and
1140 earthquakes, *J. Geophys. Res.*, 85, 3115–3121, doi:10.1029/JB085iB06p03115
- 1141 Jovovic, I., Grossi, V., Adam, P., Cartigny, P., Antheaume, I., Sala, D., Milesi, V., Jezequel, D., Ader,
1142 M., Gelin, F. (2017) Early diagenesis and preservation of sedimentary organic matter in an anoxic,
1143 sulfidic lake (Lake Dziani Dzaha, Mayotte). 28th *International Meeting on organic geochemistry* 17-
1144 22 September 2017, Florence, Italy
- 1145 Klimke, J., Franke, D., Gaedicke, C., Schreckenberger, B., Schnabel, M., Stollhofen, H., Rose, J. &
1146 Chaheire, M., 2016. How to identify oceanic crust—Evidence for a complex break-up in the
1147 Mozambique Channel, off East Africa, *Tectonophysics*, 693, 436-452
- 1148 Leboulanger, C., Agogue, H., Bernard, C., Bouvy, M., Carre, C., Cellamare, M., et al. (2017).
1149 Microbial diversity and cyanobacterial production in Dziani Dzaha crater lake, a unique tropical
1150 thalassohaline environment. *PLoS One*, 12(1), e0168879. Nehlig et al., 2013
- 1151 Lemoine, A., Briole, P., Bertil, D., Roullé, A., Fournel, M., Thinon, I., Raucoules, D., et al. (2020)
1152 The 2018–2019 seismo-volcanic crisis east of Mayotte, Comoros islands: seismicity and ground
1153 deformation markers of an exceptional submarine eruption, *Geophysical Journal International*,
1154 Volume 223, Issue 1, October 2020, Pages 22–44, <https://doi.org/10.1093/gji/ggaa273>
- 1155 Liuzzo, M., Di Muro, A., Giudice, G., Michon, L., Ferrazzini, V. and Gurrieri, S. (2015) New evidence
1156 of CO₂ soil degassing anomalies on Piton de la Fournaise volcano and the link with volcano
1157 tectonic structures. *Geochem. Geophys. Geosyst.* 16. <https://doi.org/10.1002/2015GC006032>

1158 Liuzzo, M., Gurrieri, S., Giudice, G. and Giuffrida, G. (2013) Ten years of soil CO₂ continuous
 1159 monitoring on Mt. Etna: exploring the relationship between processes of soil degassing and
 1160 volcanic activity. *Geochem. Geophys. Geosyst.* 14, 2886–2899

1161 Marty, B., Meynier, V., Nicolini, E., Griesshaber, E., and Toutain, J. P. (1993), Geochemistry of gas
 1162 emanations: A case study of the Reunion hot spot, Indian ocean, *Appl. Geochem.*, 8, 141–152

1163 Mazzini, A., Svensen, H., Etiope, E., Onderdonk, N., and Banks, D. (2011). Fluid origin, gas fluxes
 1164 and plumbing system in the sediment-hosted Salton Sea Geothermal System (California, USA). *J.*
 1165 *Volcanol. Geothermal Res.* 205, 67–83. doi: 10.1016/j.jvolgeores.2011.05.008

1166 Michon, L., 2016. The volcanism of the Comoros archipelago integrated at a regional scale. In:
 1167 Bachèlery, P., Lénat, J.-F., Di Muro, A., Michon, L. (Eds.), *Active Volcanoes of the Southwest Indian*
 1168 *Ocean: Piton de La Fournaise and Karthala. Springer-Verlag, Berlin and Heidelberg*, pp. 333–344

1169 Milesi, V. P., Debure, M., Marty, N. C. M., Capano, M., et al. (2020) Early Diagenesis of Lacustrine
 1170 Carbonates in Volcanic Settings: The Role of Magmatic CO₂ (Lake Dziani Dzaha, Mayotte, Indian
 1171 Ocean) *ACS Earth and Space Chemistry* 2020 4 (3), 363–378 DOI:
 1172 10.1021/acsearthspacechem.9b00279

1173 Milesi, V. P., Jézéquel, D., Debure, M., Cadeau, P., Guyot, F., Sarazin, G., Claret, F., Vennin, E.,
 1174 Chaduteau, C., Virgone, A., et al. (2019) Formation of Magnesium-Smectite during Lacustrine
 1175 Carbonates Early Diagenesis: Study Case of the Volcanic Crater Lake Dziani Dzaha (Mayotte- Indian
 1176 Ocean). *Sedimentology* 2019, 66, 983–1001

1177 Nehlig, P., Lacquement, F., Bernard, J., Audru, J., Caroff, M., Deparis, J., et al. (2013). Notice
 1178 explicative de la carte géologique Mayotte à 1/30.000 feuille Mayotte (1179). Orléans : BRGM, 74
 1179 p. Carte géologique par Lacquement F., Nehlig P., Bernard J. (2013).

1180 Nougier, J., Cantagrel, J.M., & Karche, J.P., 1986. The Comoros archipelago in the western Indian
 1181 Ocean: volcanology, geochronology and geodynamic setting, *Journal of African Earth Sciences* ,
 1182 5(2), 135–144

1183 Ono, A., Sano, Y., Wakita, H., Giggenbach, W. F. (1993) Carbon isotopes of methane and carbon
 1184 dioxide in hydrothermal gases of Japan, *Geochemical Journal*, Vol. 27, Issue 4-5, Pages 287–295
 1185 <https://doi.org/10.2343/geochemj.27.287>

1186 Ozima, M., and Podosek, F. A. (1983). *Noble Gas Geochemistry*. New York, NY: *Cambridge*
 1187 *University Press*

1188 Paonita, A., Caracausi, A., Martelli, M., & Rizzo, A. L. (2016) Temporal variations of helium isotopes
 1189 in volcanic gases quantify pre-eruptive refill and pressurization in magma reservoirs: The Mount
 1190 Etna case. *Geology* 44(7), 499–502

1191 Pelleter, A., Caroff, M., Cordier, C., Bachèlery, P., Nehlig, P., Debeuf, D., Arnaud, N., (2014) Melilite-
 1192 bearing lavas in Mayotte (France): an insight into the mantle source below the Comoros. *Lithos*
 1193 208–209, 281–297. <https://doi.org/10.1016/j.lithos.2014.09.012>

- 1194 Phethean, J.J.J. (2016) Madagascar's escape from Africa: a high-resolution plate reconstruction for
1195 the Western Somali Basin and implications for supercontinent dispersal. *G-Cubed* 17, 5036–5055.
1196 <https://doi.org/10.1002/2016GC006624>. Received
- 1197 Rabinowitz, P. D., Coffin, M. F., and Falvey, D. (1983) The separation of Madagascar and Africa,
1198 *Science*, 220, 67–69
- 1199 Reid, R.C., Prausnitz, J.M., and Sherwood, T.K. (1977). The properties of gases and liquids. 3rd Ed.
1200 *McGraw-Hill*
- 1201 REVOSIMA, 2019. Bulletin n°1 de l'activité sismo-volcanique à Mayotte, IPGP, Université de Paris,
1202 OVPF, BRGM, Ifremer, CNRS, August, 23th, 2019,
1203 http://www.ipgp.fr/sites/default/files/ipgp_1er_bulletin_info_sismo_volcanique_mayotte-cor.pdf
1204 and www.ipgp.fr/revosima
- 1205 Richet, P., Bottinga, Y., and Javoy, M. (1977) A review of hydrogen, carbon, nitrogen, oxygen,
1206 sulfur, and chlorine stable isotope fractionation among gaseous molecules. *Ann. Rev. Earth Planet.*
1207 *Sci.* 5, 65–110
- 1208 Rizzo, A.L., Caracausi, A., Chavagnac, V., Nomikou, P., Polymenakou, P.N., Mandalakis, M.,
1209 Kotoulas G., Magoulas, A., Castillo, A., Lampridou, D., Maruszczak, N, and Sonke, J.E. (2019)
1210 Geochemistry of CO₂-Rich Gases Venting From Submarine Volcanism: The Case of Kolumbo
1211 (Hellenic Volcanic Arc, Greece). *Front. Earth Sci.* 7:60. doi: 10.3389/feart.2019.00060
- 1212 Rizzo, A. L., Federico, C., Inguaggiato, S., Sollami, A., Tantillo, M., Vita, F., Bellomo, S., Longo, M.,
1213 Grassa, F., and Liuzzo, M. (2015) The 2014 effusive eruption at Stromboli volcano (Italy):
1214 Inferences from soil CO₂ flux and 3He/ 4He ratio in thermal waters, *Geophys. Res. Lett.*, 42, 2235–
1215 2243, doi:10.1002/2014GL062955
- 1216 Rizzo, A. L., Caracausi, A., Chavagnac, V., Nomikou, P., Polymenakou, P. N., Mandalakis, M., et al.
1217 (2016) Kolumbo submarine volcano (Greece): an active window into the Aegean subduction
1218 system. *Sci. Rep.* 6:28013. doi: 10.1038/srep28013
- 1219 Roach, P., Milsom, J., Toland, C., Matchette-Downes, C., Budden, C., Riaroh, D., And Houmadi, N.
1220 (2017) New evidence supports presence of continental crust beneath the Comoros: *Pesgb/Hgs*
1221 *Africa Conference*. Aug 2017
- 1222 Rouff, A. A., Phillips, B. L., Cochiara, S. G., and Nagy, K. L. (2012) The Effect of dissolved humic acids
1223 on aluminosilicate formation and associated carbon sequestration, *Appl. Environ. Soil Sci.*, 2012,
1224 12, doi:10.1155/2012/430354
- 1225 Sanjuan, B., Baltassat, J., Bezelgues, S., Brach, M., Girard, J., & Mathieu, F. (2008). Estimation du
1226 potentiel géothermique de Mayotte: Phase 2-Étape 2. Investigations géologiques, géochimiques et
1227 géophysiques complémentaires, synthèse des résultats. Rapport BRGM/RP-56802-FR, 82 p., 18
1228 fig., 3 tabl., 6 ann.
- 1229 Sano, Y., and Wakita, H. (1985) Distribution of 3He/4He ratios and its implications for geotectonic
1230 structure of the Japanese Islands. *J. Geophys. Res.* 90, 8729-8741

- 1231 Sano, Y., and Marty, B. (1995). Origin of carbon in fumarolic gases from island arcs. *Chem. Geol.*
1232 119, 265–274. doi: 10.1016/0009-2541(94)00097-R
- 1233 Sano, Y., Kagoshima, T., Takahata, N., et al. Ten-year helium anomaly prior to the 2014 Mt Ontake
1234 eruption. *Sci Rep* 5, 13069 (2015). <https://doi.org/10.1038/srep13069>
- 1235 Schoell, M. (1980). The hydrogen and carbon isotopic composition of methane from natural gases
1236 of various origins. *Geochim. Cosmochim. Acta* 44, 649–661. doi: 10.1016/0016-7037(80)90155-6
- 1237 Severinghaus, J.P., Bender, M.L., Keeling, R.F., Broecker, W.S. (1996) Fractionation of soil gases by
1238 diffusion of water vapor, gravitational settling and thermal diffusion. *Geochim Cosmochim Acta*
1239 60:1005–1018
- 1240 Späth, A., Roex, A. P. L., & Duncan, R. A. (1996). The Geochemistry of Lavas from the Gomores
1241 Archipelago, Western Indian Ocean: Petrogenesis and Mantle Source Region Characteristics.
1242 *Journal of Petrology*, 37(4), 961-991.
- 1243 Taran, Y. A., Kliger, G. A., Cienfuegos, E., and Shuykin, A. N. (2010). Carbon and hydrogen isotopic
1244 compositions of products of open-system catalytic hydrogenation of CO₂: implications for
1245 abiogenic hydrocarbons in Earth's crust. *Geochim. Cosmochim. Acta* 74, 6112–6125. doi:
1246 10.1016/j.gca.2010.08.012
- 1247 Traineau, H., Sanjuan, B., Brach, M., Audru, J-C. (2006) Etat des connaissances du potentiel
1248 géothermique de Mayotte. Rapport final. BRGM/RP-54700-FR
- 1249 Tzevahirtzian, A., Zaragosi, S., Bachèlery, P., Biscara, L., & Marchès, E. (2021) Submarine
1250 morphology of the Comoros volcanic archipelago. *Marine Geology*, 432, 106383.
- 1251 Welhan, J. A. (1988) Origins of methane in hydrothermal systems. *Chem. Geol.* 71, 183–198. doi:
1252 10.1016/0009-2541(88)90114-3
- 1253 Zinke, J., Reijmer, J. J. G., & Thomassin, B. A. (2001) Seismic architecture and sediment distribution
1254 within the Holocene barrier reef–lagoon complex of Mayotte (Comoro archipelago, SW Indian
1255 Ocean). *Palaeogeography, Palaeoclimatology, Palaeoecology*, 175(1-4), 343-368.
- 1256

1257
1258

Table 2 – Soil CO₂ flux (g m⁻² d⁻¹) surveys at Grande Comore and Mayotte

Grande Comore 2014			CO2 flux [g/(m ² day)]	Grande Comore 2014			CO2 flux [g/(m ² day)]	Grande Comore 2014			CO2 flux [g/(m ² day)]	Grande Comore 2014			CO2 flux [g/(m ² day)]
Latitude		Longitude		Latitude		Longitude		Latitude		Longitude		Latitude		Longitude	
		-	0.00			-				-				-	
1	11.760030	43.358620		24	11.756920	43.359290	4.00	46	11.731600	43.356970	0.00	69	11.735350	43.361070	3.20
2	11.760120	43.358940	992.60	25	11.757020	43.360120	1.30	47	11.728210	43.356650	2.50	70	11.735510	43.362140	1.30
3	11.760440	43.359140	0.00	26	11.756930	43.361020	4.60	48	11.727900	43.357430	2.60	71	11.735580	43.362880	3.00
4	11.760070	43.359300	0.00	27	11.756870	43.361130	9811.10	49	11.728070	43.358410	1.10	72	11.735400	43.361130	0.00
5	11.760150	43.359830	5378.00	28	11.756960	43.361920	0.00	50	11.727990	43.359880	1.50	73	11.734460	43.361040	0.00
6	11.760410	43.360290	8.90	29	11.756930	43.362760	0.00	51	11.728090	43.360430	1.40	74	11.733640	43.360980	1.30
7	11.760550	43.361020	0.00	30	11.753250	43.364720	0.00	52	11.728050	43.361270	1.90	75	11.732860	43.360950	1.60
8	11.760560	43.361840	0.00	31	11.753290	43.363780	0.00	53	11.727940	43.362010	4.70	76	11.731890	43.360570	5.80
9	11.760500	43.362970	0.00	32	11.753240	43.362890	0.00	54	11.728060	43.363120	9.10	77	11.730180	43.359770	6.30
10	11.760040	43.363590	0.00	33	11.753270	43.361690	0.00	55	11.728050	43.363840	3.60	78	11.729260	43.359940	1.80
11	11.758290	43.362920	30.20	34	11.753660	43.360930	0.00	56	11.727720	43.364480	3.80	79	11.728800	43.360780	1.60
12	11.758200	43.362060	0.00	35	11.753490	43.359830	0.00	57	11.732320	43.363310	21.50	80	11.730240	43.360810	4.80
13	11.757630	43.361340	1242.70	36	11.749920	43.361890	0.00	58	11.732320	43.363260	796.70	81	11.730710	43.361680	4.80
14	11.758260	43.361440	5.70	37	11.749930	43.361090	0.00	59	11.732820	43.362400	0.00	82	11.731120	43.362160	6.60
15	11.758390	43.360850	24.50	38	11.750010	43.360040	0.00	60	11.731670	43.362060	10.10	83	11.733480	43.362250	2.10
16	11.758310	43.360750	153.50	39	11.749950	43.359240	0.00	61	11.731540	43.361200	6.10	84	11.734470	43.362340	6.70
17	11.758460	43.360220	7.90	40	11.749550	43.358340	0.00	62	11.731630	43.360350	3.30	85	11.734260	43.363090	3.40
18	11.758430	43.359810	0.00	41	11.753260	43.355550	0.00	63	11.731850	43.359590	7.20	86	11.733520	43.363050	2.70
19	11.758320	43.359130	21.30	42	11.753240	43.359270	0.00	64	11.731530	43.357740	4.10	87	11.732700	43.363090	8.50
20	11.758320	43.359790	6931.00	43	11.753320	43.358290	0.00	65	11.735020	43.357890	5.30	88	11.731730	43.363020	2.80
21	11.756940	43.356410	0.00	44	11.753340	43.357310	0.00	66	11.735290	43.358390	8.10	89	11.731340	43.363770	6.00
22	11.756960	43.357310	0.00	45	11.734620	43.356290	0.00	67	11.735430	43.359460	4.90	90	11.731630	43.364810	8.20
23	-	43.358240	0.00					68	-	43.360180	8.00				

Grande Comore 2014			CO2 flux [g/(m ² day)]
	Latitude	Longitude	
91	11.732660	43.364940	6.10
92	11.733500	43.365130	7.50
93	11.734420	43.364980	1.30
94	11.735480	43.365060	2.90
95	11.735480	43.364010	5.40
96	11.734120	43.364140	313.40
97	11.733950	43.364120	8994.00
98	11.733710	43.364130	553.70
99	11.733580	43.364050	175.80
100	11.733390	43.363960	3046.10
101	11.732920	43.363410	17364.40
102	11.732400	43.363310	396.10
103	11.735470	43.365470	4.50
104	11.735410	43.366680	4.20
105	11.735290	43.367860	1.60
106	11.734920	43.368590	2.70
107	11.734950	43.369160	1.50
108	11.735100	43.370020	1.30
109	11.734880	43.371330	4.30
110	11.734890	43.372370	0.00
111	11.731630	43.372480	5.30
112	11.727760	43.371830	2.70
113	11.728050	43.370230	3.00
114	11.728340	43.369200	13.50
115	43.368350		1.30

Grande Comore 2014			CO2 flux [g/(m ² day)]
	Latitude	Longitude	
5	11.728570		
11	-		2.60
6	11.728670	43.367390	
11	-		5.70
7	11.728860	43.366670	
11	-		4.80
8	11.728690	43.365970	
11	-		4.40
9	11.728840	43.365040	
12	-		0.00
0	11.729510	43.365180	
12	-		9.00
1	11.730080	43.365400	
12	-		1.20
2	11.731050	43.365570	
12	-		5.50
3	11.731370	43.366580	
12	-		0.50
4	11.731860	43.367570	
12	-		4.00
5	11.731190	43.368440	
12	-		1.10
6	11.731050	43.369530	
12	-		3.00
7	11.731810	43.370240	
12	-		2.20
8	11.732570	43.370970	
12	-		4.40
9	11.738900	43.372030	
13	-		4.20
0	11.738920	43.371310	
13	-		1.60
1	11.738890	43.370270	
13	-		2.70
2	11.738950	43.369280	
13	-		1.50
3	11.738940	43.368460	
13	-		1.30
4	11.738900	43.367580	
13	-		4.20
5	11.738890	43.366800	
13	-		0.00
6	11.738880	43.365750	
13	-		2.50
7	11.738770	43.365270	
13	-		1.10
8	11.738960	43.363820	
13	-		1.50
9	11.738840	43.363260	

1259

Grande Comore 2014			CO2 flux [g/(m ² day)]
	Latitude	Longitude	
14	-		1.40
0	11.739020	43.361900	
14	-		1.90
1	11.738830	43.361170	
14	-		4.60
2	11.738850	43.360300	
14	-		8.90
3	11.738890	43.359250	
14	-		3.60
4	11.738860	43.358360	
14	-		3.70
5	11.738570	43.357640	
14	-		21.10
6	11.738800	43.356490	
14	-		1.30
7	11.742410	43.360250	
14	-		2.20
8	11.742630	43.361150	
14	-		2.90
9	11.742560	43.362230	
15	-		7.20
0	11.742500	43.363040	
15	-		3.30
1	11.742550	43.363730	
15	-		6.00
2	11.742620	43.364710	
15	-		10.00
3	11.742450	43.365780	
15	-		0.00
4	11.742530	43.366600	
15	-		7.80
5	11.742480	43.367530	

Grande Comore 2017			CO2 flux [g/(m ² day)]
	Latitude	Longitude	
1	11.579000	43.311000	32.10
2	11.525000	43.337000	15.10
3	11.879000	43.407000	22.66
4	11.872000	43.399000	18.88
5	11.735000	43.329000	18.88
6	11.735000	43.329000	47.20
7	11.734000	43.328000	33.98
8	11.733000	43.327000	18.88
9	11.732000	43.326000	52.86
10	11.731000	43.326000	45.31
11	11.730000	43.324000	16.99
12	11.728000	43.323000	22.66
13	11.723000	43.250000	24.54
14	11.725000	43.249000	168.07
15	11.727000	43.250000	239.87
16	11.730000	43.250000	32.10
17	11.730000	43.249000	20.77
18	11.732000	43.250000	30.21
19	11.734000	43.249000	33.98
20	11.737000	43.250000	24.54
21	11.720000	43.249000	13.22
22	11.849000	43.332000	20.77
23	11.849000	43.330000	256.89
24	11.849000	43.328000	41.54
25	-	43.328000	98.18

Grande Comore 2017			CO2 flux [g/(m ² day)]
	Latitude	Longitude	
26	11.848000	43.321000	18.88
27	11.847000	43.316000	49.09
28	11.846000	43.314000	79.30
29	11.847000	43.311000	54.75
30	11.846000	43.306000	179.40
31	11.844000	43.303000	22.66
32	11.842000	43.301000	18.88
33	11.840000	43.299000	18.88
34	11.837000	43.297000	11.33
35	11.833000	43.292000	120.84
36	11.829000	43.288000	145.40
37	11.784000	43.271000	30.21
38	11.780000	43.267000	226.64
39	11.778000	43.265000	160.51
40	11.775000	43.264000	457.58
41	11.719000	43.249000	16.99
42	11.721000	43.245000	22.66
43	11.723000	43.245000	16.99
44	11.727000	43.244000	60.42
45	11.728000	43.243000	22.66
46	11.728000	43.240000	22.66
47	11.730000	43.242000	15.10
48	11.733000	43.241000	226.64
49	11.735000	43.240000	118.96

Grande Comore 2017			CO2 flux [g/(m ² day)]
	Latitude	Longitude	
50	11.737000	43.240000	94.41
51	11.740000	43.240000	43.42
52	11.742000	43.239000	16.99
53	11.747000	43.238000	22.66
54	11.748000	43.235000	50.98
55	11.752000	43.236000	52.86
56	11.759000	43.239000	11.33
57	11.759000	43.244000	37.76
58	11.560000	43.273000	9.44
59	11.566000	43.272000	94.41
60	11.570000	43.271000	13.221260
61	11.577000	43.269000	18.88
62	11.584000	43.267000	35.87
63	11.588000	43.266000	103.85
64	11.592000	43.266000	109.51
65	11.597000	43.263000	11.33
66	11.609000	43.263000	13.22
67	11.629000	43.307000	20.77
68	11.626000	43.309000	306.06
69	11.622000	43.312000	20.77
70	11.618000	43.314000	135.95
71	11.616000	43.315000	62.31
72	11.594000	43.378000	147.29
73	11.591000	43.382000	16.99
74	-	43.404000	98.18

Grande Comore 2017			CO2 flux [g/(m ² day)]
	Latitude	Longitude	
75	11.427000	43.399000	39.65
76	11.438000	43.399000	120.84
77	11.447000	43.402000	100.07
78	11.454000	43.402000	22.66
79	11.610000	43.365000	16.99
80	11.612000	43.363000	228.53
81	11.614000	43.357000	24.54
82	11.613000	43.350000	24.54
83	11.610000	43.346000	71.75
84	11.611000	43.341000	13.22

Grande Comore 2018			CO2 flux [g/(m ² day)]
	Latitude	Longitude	
1	11.876616	43.480066	7.55
2	11.878802	43.481346	7.55
3	11.879880	43.477517	13.22
4	11.879253	43.472302	7.55
5	11.882023	43.469274	13.22
6	11.885114	43.468817	9.44
7	11.884848	43.465353	11.33
8	11.885446	43.457200	7.55
9	11.886513	43.452216	18.88
10	11.888558	43.445997	28.32
11	-	43.442657	33.98

Grande Comore 2018			CO2 flux [g/(m ² day)]
	Latitude	Longitude	
	11.890019	-	
12	11.890607	43.440029	22.66
	-	-	
13	11.893221	43.435186	20.77
	-	-	
14	11.894565	43.430336	28.32
	-	-	
15	11.756312	43.355270	7.55
	-	-	
16	11.758078	43.357018	9.44
	-	-	
17	11.757963	43.357585	7.55
	-	-	
18	11.757925	43.357977	9.44
	-	-	
19	11.758013	43.358559	9.44
	-	-	
20	11.757705	43.358812	7.55
	-	-	
21	11.757610	43.359170	16.99
	-	-	
22	11.757605	43.359566	30.21
	-	-	
23	11.757513	43.359916	22.66
	-	-	
24	11.757327	43.360275	11.33
	-	-	
25	11.757155	43.360631	802.29
	-	-	
26	11.757020	43.360974	951.98
	-	-	
27	11.756931	43.361213	45.31
	-	-	
28	11.756826	43.361449	283.36
	-	-	
29	11.756816	43.361700	32.10
	-	-	
30	11.756957	43.362062	9.44
	-	-	
31	11.757067	43.362450	7.55
	-	-	
32	11.757152	43.362882	7.55
	-	-	
33	11.732509	43.363215	15.10
	-	-	
34	11.637843	43.376308	11.33
	-	-	
35	11.636014	43.375007	22.66

Grande Comore 2018			CO2 flux [g/(m ² day)]
	Latitude	Longitude	
	-	-	
36	11.634025	43.373187	7.55
	-	-	
37	11.632313	43.371923	7.55
	-	-	
38	11.628818	43.372358	9.44
	-	-	
39	11.628904	43.372267	13.22
	-	-	
40	11.627732	43.368685	9.44
	-	-	
41	11.627151	43.365583	7.55
	-	-	1261
42	11.622232	43.365063	5.66
	-	-	
43	11.619964	43.363529	5.66
	-	-	
44	11.615842	43.359638	47.20
	-	-	
45	11.614397	43.355913	7.55
	-	-	
46	11.613988	43.352644	7.55
	-	-	
47	11.613266	43.350659	16.99
	-	-	
48	11.611125	43.349181	30.21
	-	-	
49	11.609914	43.345950	11.33
	-	-	
50	11.612037	43.338725	28.32
	-	-	
51	11.613682	43.333515	9.44
	-	-	
52	11.614027	43.329282	7.55
	-	-	
53	11.614261	43.324552	9.44
	-	-	
54	11.614549	43.322405	20.77
	-	-	
55	11.614855	43.317845	20.77
	-	-	
56	11.615610	43.314634	16.99
	-	-	
57	11.618371	43.313629	28.32
	-	-	
58	11.621824	43.312271	9.44
	-	-	
59	11.626042	43.308930	105.74
60	-	43.309033	56.64

Grande Comore 2018			CO2 flux [g/(m ² day)]
Latitude	Longitude		
	11.625871	-	
61	11.626137	43.308888	120.84
		-	
62	11.780161	43.267323	67.97
		-	
63	11.770174	43.261717	11.33
		-	
64	11.759701	43.256409	37.76
		-	
65	11.758396	43.242995	84.96

Mayotte 2019			CO2 flux [g/(m ² day)]
Latitude	Longitude		
1	45.286856	-12.799818	50.66
2	45.286886	-12.799780	3.50
3	45.286808	-12.799860	7.62
4	45.286780	-12.799913	4.02
5	45.286777	-12.799973	9.68
6	45.286748	-12.799982	5.70
7	45.286731	-12.800008	5.66
8	45.286717	-12.800075	3.90
9	45.286699	-12.800123	4.26
10	45.286686	-12.800178	3.95
11	45.286703	-12.800208	30.90
12	45.286661	-12.800261	2.92
13	45.286664	-12.800280	4.80
14	45.286682	-12.800339	2.04
15	45.286693	-12.800380	0.52
16	45.286672	-12.800439	1.64
17	45.286711	-12.800493	2.28
18	45.285713	-12.800167	5.28
19	45.285764	-12.800136	4.86
20	45.285806	-12.800110	12.65
21	45.285844	-12.800085	8.40
22	45.285883	-12.800070	17.57
23	45.285907	-12.800087	5.70
24	45.286072	-12.800006	22.82
25	45.286160	-12.800000	9.00
26	45.286118	-12.799945	17.06
27	45.286107	-12.799880	7.76
28	45.286142	-12.799805	5.36
29	45.286244	-12.799578	21.54

Mayotte 2019			CO2 flux [g/(m ² day)]
Latitude	Longitude		
30	45.286335	-12.799336	41.57
31	45.286491	-12.799352	14.70
32	45.286694	-12.799469	19.13
33	45.286883	-12.799525	6.48
34	45.287022	-12.799293	11.90
35	45.287079	-12.799116	8.10
36	45.287149	-12.798782	12.95
37	45.282678	-12.805537	0.45
38	45.282875	-12.805612	1.18
39	45.283069	-12.805955	0.00
40	45.282586	-12.805040	1.63
41	45.282379	-12.805167	1.00
42	45.277490	-12.802276	0.00
43	45.277386	-12.802210	0.00
44	45.277352	-12.802227	0.00
45	45.277246	-12.802167	4.45
46	45.277162	-12.802143	4.36
47	45.277292	-12.802176	1.21
48	45.277152	-12.802055	8.00
49	45.277126	-12.801957	1.64
50	45.277061	-12.801850	0.52
51	45.276823	-12.801281	15.70
52	45.276858	-12.801248	4.21
53	45.284543	-12.799820	11.56
54	45.284848	-12.799386	37.94
55	45.284923	-12.799228	173.44
56	45.285052	-12.799154	39.81
57	45.285033	-12.797719	0.00
58	45.285041	-12.797734	11.98
59	45.284897	-12.797933	4.84
60	45.284909	-12.798320	27.11
61	45.284959	-12.798641	13.28
62	45.284912	-12.798811	42.42
63	45.284776	-12.799008	9.62
64	45.285290	-12.797520	1.69
65	45.285442	-12.797118	2.12
66	45.285659	-12.796799	6.87
67	45.284645	-12.801006	2.36
68	45.284708	-12.800662	3.18
69	45.286793	-12.800945	3.26
70	45.288012	-12.799281	2.55
71	45.287850	-12.799243	0.49
72	45.287528	-12.799367	0.00
73	45.287306	-12.799543	4.04
74	45.287123	-12.799624	1.61

Mayotte 2019			CO2 flux [g/(m ² day)]
Latitude	Longitude		
75	45.281475	-12.795606	1.99
76	45.281311	-12.796021	4.06
77	45.281218	-12.796457	6.18
78	45.281190	-12.797037	6.81
79	45.281312	-12.797480	2.53
80	45.281154	-12.798122	2.03
81	45.280780	-12.798222	7.22
82	45.281349	-12.797331	2.60
83	45.282582	-12.798498	5.60
84	45.282209	-12.799108	1.80
85	45.280079	-12.792672	1.06
86	45.279778	-12.793405	1.45
87	45.279577	-12.794203	3.39
88	45.279207	-12.795135	13.83
89	45.279342	-12.795964	0.00
90	45.278689	-12.796682	3.46
91	45.278386	-12.797120	2.67
92	45.278279	-12.797905	16.76
93	45.277967	-12.798124	0.00
94	45.277448	-12.798648	7.81
95	45.255220	-12.782986	1.97
96	45.255288	-12.781948	3.81
97	45.254958	-12.781035	0.00
98	45.257887	-12.783449	2.11
99	45.260400	-12.785424	3.47
10			
0	45.261339	-12.786133	2.61
10			
1	45.262178	-12.786088	0.00
10			
2	45.261778	-12.785416	3.32
10			
3	45.264903	-12.787605	5.05
10			
4	45.268356	-12.789905	5.71
10			
5	45.268894	-12.791590	2.73
10			
6	45.273430	-12.794984	8.00
10			
7	45.274379	-12.794448	5.34
10			
8	45.275029	-12.794076	1.03
10			
9	45.275483	-12.793842	2.43
11			
0	45.275939	-12.793916	7.21

Mayotte 2019			CO2 flux [g/(m ² day)]
Latitude	Longitude		
11			
1	45.276297	-12.793910	12.45
11			
2	45.276781	-12.793827	3.11
11			
3	45.277189	-12.793428	2.68
11			
4	45.277539	-12.792994	1.97
11			
5	45.278188	-12.792446	5.57
11			
6	45.280727	-12.766360	0.00
11			
7	45.280762	-12.768051	0.39
11			
8	45.279645	-12.770106	2.52
11			
9	45.279858	-12.771997	3.38
12			
0	45.280814	-12.774220	2.93
12			
1	45.281827	-12.776119	1.50
12			
2	45.294567	-12.783769	1.70
12			
3	45.293457	-12.784258	6.53
12			
4	45.292021	-12.784650	3.35
12			
5	45.290841	-12.785500	26.03
12			
6	45.289486	-12.785186	6.06
12			
7	45.288814	-12.784143	10.06
12			
8	45.288652	-12.783974	11.54
12			
9	45.289141	-12.783073	6.76
13			
0	45.288129	-12.782416	1.27
13			
1	45.286670	-12.781859	4.26
13			
2	45.285204	-12.782200	0.00
13			
3	45.283348	-12.782728	6.09
Mayotte Bubbling Area Sea 2019			CO2 flux

Mayotte 2019			CO2 flux [g/(m ² day)]
Latitude	Longitude		
			[g/(m ² day)]
			33304.
1	45.288840	-12.800657	40
			33304.
2	45.288840	-12.800657	40
			29549.
3	45.288818	-12.800576	64
			29549.
4	45.288818	-12.800576	64
			20025.
5	45.288787	-12.800533	38
			20025.
6	45.288787	-12.800533	38
			21481.
7	45.288766	-12.800518	59
			21481.
8	45.288766	-12.800518	59
			21481.
9	45.288766	-12.800518	59
			21481.
10	45.288766	-12.800518	59
			34896.
11	45.288734	-12.800502	13
			34896.
12	45.288734	-12.800502	13
			22764.
13	45.288676	-12.800483	99
			27874.
14	45.288611	-12.800534	64
			12330.
15	45.288257	-12.799866	93
			12330.
16	45.288257	-12.799866	93
			12330.
17	45.288257	-12.799866	93
			12330.
18	45.288257	-12.799866	93
			12330.
19	45.288257	-12.799866	93
			12330.
20	45.288257	-12.799866	93
			12330.
21	45.288257	-12.799866	93
			12330.
22	45.288257	-12.799866	93
			12330.
23	45.288257	-12.799866	93
24	45.288257	-12.799866	12330.

Mayotte 2019			CO2 flux [g/(m ² day)]
Latitude	Longitude		
			93
			12330.
25	45.288257	-12.799866	93
			12330.
26	45.288257	-12.799866	93
			35046.
27	45.287666	-12.800374	24
			35046.
28	45.287666	-12.800374	24
			35046.
29	45.287666	-12.800374	24
			35046.
30	45.287666	-12.800374	24
			35046.
31	45.287666	-12.800374	24
			35046.
32	45.287666	-12.800374	24
			18028.
33	45.287361	-12.800153	15
			18028.
34	45.287361	-12.800153	15
			18028.
35	45.287361	-12.800153	15
			18028.
36	45.287361	-12.800153	15
			47932.
37	45.287364	-12.800154	23
			12824.
38	45.287370	-12.800155	78
			13008.
39	45.287392	-12.800154	43
			18762.
40	45.287356	-12.800126	74
			18762.
41	45.287356	-12.800126	74
			23629.
42	45.287388	-12.800106	43
			23629.
43	45.287388	-12.800106	43
			23629.
44	45.287388	-12.800106	43
45	45.287402	-12.800144	136.21
			35046.
46	45.288553	-12.800236	24
			70485.
47	45.289069	-12.800259	66
			17064.
48	45.289104	-12.800310	31
49	45.289178	-12.800359	26435.

Mayotte 2019			CO2 flux [g/(m² day)]
Latitude	Longitude		
			94
50	45.289290	-12.800481	8730.58
51	45.289524	-12.800485	5952.67
52	45.289584	-12.800270	15537.98
53	45.289039	-12.800000	14289.19

1262

1263

Mayotte 2020			CO2 flux [g/(m ² day)]
Latitude	Longitude		
1	45.28444	-12.7644	4.81
2	45.28326	-12.7654	6.69
3	45.28096	-12.7656	5.95
4	45.28058	-12.7681	15.93
5	45.27964	-12.7702	34.82
6	45.27978	-12.7718	17.22
7	45.28066	-12.7736	26.00
8	45.28116	-12.7753	17.04
9	45.28222	-12.7771	13.72
10	45.28137	-12.7787	16.14
11	45.28062	-12.7801	15.93
12	45.27904	-12.7812	29.44
13	45.27759	-12.7818	39.00
14	45.27644	-12.7828	8.52
15	45.27516	-12.7842	4.78
16	45.27395	-12.7852	48.00
17	45.27289	-12.7863	8.96
18	45.26905	-12.7873	10.93
19	45.26936	-12.7895	19.95
20	45.26946	-12.7896	3.85
21	45.26819	-12.789	7.94
22	45.2847	-12.7824	62.91
23	45.28392	-12.7826	159.30
24	45.28293	-12.7828	28.73
25	45.28168	-12.783	6.07
26	45.28016	-12.7838	48.72
27	45.27952	-12.7842	14.55
28	45.27929	-12.7856	13.95
29	45.2793	-12.7856	37.36
30	45.27905	-12.7868	4.03
31	45.27994	-12.7891	15.85
32	45.28001	-12.7911	12.56
33	45.28612	-12.7999	29.08

1264

1265

1266

1267 Table 3 – Synopsis of soil CO₂ results and relative method used and year of measurements

CO ₂ flux [g m ⁻² day ⁻¹]	Grande Comore		Grande Comore		Mayotte		Mayotte Bubbling Sea
	2014		2017	2018	2019	2020	2019
Min	0.0		9.44	5.66	0.0	3.85	12.2
Max	17364.4		457.58	951.98	173.4	159.3	70485.7
Average	365.6		67.61	51.91	8.2	23.90	21084.0
σ	1886.3		79.41	153.91	17.0	28.39	12045.2
Accumulation Chamber			Dynamic Concentration (K=30)		Accumulation Chamber		Accumulation Chamber

1268

1269

1270

1271